

AD A 022 955

AFCRL-TR-76-0057
ENVIRONMENTAL RESEARCH PAPERS. NO. 550
HAES REPORT NO. 38

12



Rocket Measurement of OH Emission Profiles in the 1.56 and 1.99 μ m Bands

W. F. GRIEDER
K. D. BAKER
A. T. STAIR, Jr.
J. C. ULWICK

28 January 1976

DDC
RECEIVED
APR 14 1976
C

Approved for public release; distribution unlimited.

OPTICAL PHYSICS LABORATORY PROJECT 7670
AIR FORCE CAMBRIDGE RESEARCH LABORATORIES
HANSCOM AFB, MASSACHUSETTS 01731

AIR FORCE SYSTEMS COMMAND, USAF



DTIC
 DDC
 UNCLASSIFIED
 JUSTIFICATION
 BY SECTION/AVAILABILITY CODES
 A

Work Section ☒
 Edit Section ☐

Qualified requestors may obtain additional copies from the Defense Documentation Center. All others should apply to the National Technical Information Service.

Unclassified

SECURITY CLASSIFICATION OF THIS PAGE (When Data Entered)

REPORT DOCUMENTATION PAGE		HEAD INSTRUCTIONS BEFORE COMPLETING FORM	
1. REPORT NUMBER	2. GOVT ACCESSION NO.	3. RECIPIENT'S CATALOG NUMBER	
AFCRL-TR-76-0057, AFRL-ERP-350			
4. TITLE (and Subtitle)		5. TYPE OF REPORT & PERIOD COVERED	
ROCKET MEASUREMENT OF OH EMISSION PROFILES IN THE 1.56 AND 1.99 μm BANDS,		Scientific, Interim.	
7. AUTHOR		6. PERFORMING ORG. REPORT NUMBER	
W.F. Grieder* A.T. Stair, Jr. K.D. Baker* J.C. Ulwick		ERP No. 550	
9. PERFORMING ORGANIZATION NAME AND ADDRESS		8. CONTRACT OR GRANT NUMBER(s)	
Air Force Cambridge Research Laboratories(OP) Hanscom AFB Massachusetts 01731		micrometer	
10. PROGRAM ELEMENT, PROJECT, TASK AREA & WORK UNIT NUMBERS		11. CONTROLLING OFFICE NAME AND ADDRESS	
62101F 16 AF-7670 10 01 967010		Air Force Cambridge Research Laboratories(OP) Hanscom AFB Massachusetts 01731	
12. REPORT DATE		13. NUMBER OF PAGES	
28 Jan 1976		73	
14. MONITORING AGENCY NAME & ADDRESS (if different from Controlling Office)		15. SECURITY CLASS. (of this report)	
		Unclassified	
16. DISTRIBUTION STATEMENT (of this Report)		15a. DECLASSIFICATION/DOWNGRADING SCHEDULE	
Approved for public release; distribution unlimited.			
17. DISTRIBUTION STATEMENT (of the abstract entered in Block 20, if different from Report)			
9 Environmental research paper			
18. SUPPLEMENTARY NOTES			
*Utah State University Logan, Utah 84322			
19. KEY WORDS (Continue on reverse side if necessary and identify by block number)			
OH emission SWIR backgrounds D region aeronomy Infrared (λ = 990 nm)			
20. ABSTRACT (Continue on reverse side if necessary and identify by block number)			
Results of radiometer measurements of infrared Hydroxyl (OH) emissions from five rocket flights are presented. Two of the rocket payloads were flown from Poker Flat Rocket Range, Alaska and three were flown from White Sands Missile Range, New Mexico. Four of the flights were flown during nighttime conditions and one (at WSMR) was flown during twilight (λ = 990 nm). Each rocket payload was instrumented with liquid nitrogen cooled dual-channel radiometers to measure infrared OH emissions from the vibration-rotation bands 2-0 through 5-3 (1.56 μm channel) and the 7-5 through 9-7			

DD FORM 1 JAN 73 1473

EDITION OF 1 NOV 65 IS OBSOLETE

Unclassified

SECURITY CLASSIFICATION OF THIS PAGE (When Data Entered)

12 76p.

11 507

CON 4-0

Unclassified

SECURITY CLASSIFICATION OF THIS PAGE(When Data Entered)

20. Abstract (Continued)

(1.99 μm channel). The rocket data shows that the principle OH emissions in the bands cited occurs in a thin layer 8 to 10 km thick with peak emission near an altitude of 89 km. The ratio of nighttime 1.56 μm to 1.99 μm radiance is constant, at a value of 1.4, up to an altitude of 80 km regardless of latitude. At twilight, this ratio is larger at low altitudes (60 km) and diminishes with increasing altitude. Estimated nighttime peak volume emission rates at WSMR are 1 megaphotons $\text{cm}^{-3} \text{sec}^{-1} \mu\text{m}^{-1}$ in the 1.56 μm band and 0.7 megaphotons $\text{cm}^{-3} \text{sec}^{-1} \mu\text{m}^{-1}$ in the 1.99 μm band.

micrometer
per cm per sec per micrometer
per cm per sec per micrometer

Unclassified

SECURITY CLASSIFICATION OF THIS PAGE(When Data Entered)

Foreword

A High Altitude Effects Simulation (HAES) program is being conducted by the Defense Nuclear Agency. Under HAES, several related but distinct measurement programs have been or will be conducted to provide information for development and test of predictive computer codes which are used to assess and evaluate the operation of critical DOD radar and optical infrared systems in nuclear disturbed environments. The Air Force Cambridge Research Laboratories work under the HAES program will be reported under the HAES Series, AFCRL Environmental Research Papers. The reports will also identify the measurement program (for example, ICECAP, EXCEDE, SPIRE, etc.) so that related reports and results can be correlated and utilized. One of the measurement programs, ICECAP (Infrared Chemistry Experiments - Coordinated Auroral Program), is conducted in the polar disturbed atmosphere. The specific objective of ICECAP is to execute coordinated field measurement programs to investigate ionization and excitation mechanisms and chemical processes leading to both short and long wavelength infrared (SWIR, 1 to 6 μm and LWIR, 6 to 30 μm) emissions in an auroral display. The measurements are coordinated utilizing rocket, balloon, aircraft and ground-based observational platforms where appropriate. The program has at present three distinct phases: (1) Observation of infrared and related emissions along with production sources and ionospheric measurements in bright auroral arcs; (2) Observations of infrared aurorally associated emissions during daylight; and (3) Observations of hydroxyl (OH) auroral enhancements.

The report presents rocket measurements of infrared emissions in the vibration-rotation bands of the hydroxyl (OH) molecule in both mid-latitude and auroral zones. Particular emphasis is given to data reduction procedures, correction of

data for rocket aspect, and computation of OH volume emission rates. A concerted effort is made to present all pertinent information necessary for other analysts to utilize the measured data for individual studies.

A. T. STAIR, JR.

JAMES C. ULWICK

Preface

The authors wish to express appreciation to the many scientists, engineers, program directors, computer programmers, and other technical personnel that were responsible for the design and calibration of the rocket instruments, execution of the field program, reduction of the data, and preparation of this report. In particular, we wish to commend the efforts of Messr. Larry Jensen and John Kemp, payload and instrument engineers at Utah State University; Dr. Clair Wyatt, Doran Baker (all of USU) for technical guidance and program direction; Robert E. McInerney, John Kotelly, and Edward Robinson of the data processing system used in rendering the data and Messr. Dennis Dolorey, Niel Grossbard and Mrs. Carol Foley of the Space Data Analysis Laboratory, Boston College, Boston, Massachusetts, for developing and implementing data analysis routines used in the data processing system. In addition, appreciation is extended to Mrs. Gloria Foss for her superior effort in the technical typing of the manuscript and to Mr. Glenn Allred and staff for editing and compiling the report.

PRECEDING PAGE BLANK-NOT FILMED

List of Contributors

SCIENTISTS & ENGINEERS

D. J. Baker
K. D. Baker
D. Delorey
C. Foley
W. F. Grieder
N. Grossbard
L. L. Jensen
J. C. Kemp
J. Kotelly
R. E. McInerney
E. Robinson
A. T. Stair
C. L. Wyatt

Contents

1. INTRODUCTION	13
2. INSTRUMENTATION	14
2.1 Rocket Payload Configuration	14
2.2 Ground-Based Instrumentation	18
3. ROCKET FLIGHT SUMMARY	18
3.1 Rocket Flight Characteristics	18
3.2 Launch Conditions and Payload Performance	21
4. ROCKET DATA PROCESSING	25
4.1 Digitization of Data	25
4.2 Measured Altitude Emission Profiles	30
4.3 Magnetometer Aspect Data Reduction	32
5. DISCUSSION	36
5.1 Intensity Ratio Profiles	36
5.2 Volume Emission Rates	38
6. CONCLUSIONS	45
REFERENCES	47
APPENDIX A: Selected Rocket Instrument Parameters	49
APPENDIX B: Tabulations of Rocket A030.311-3 Data	55
APPENDIX C: Rocket Aspect From Magnetometer Data	61
APPENDIX D: Derivative Using Numerical Filtering	71

Illustrations

1. Schematic of Liquid Nitrogen Cooled OH Radiometer	15
2. Astrobee D Rocket Payload Configuration	16
3. Radiometer Relative System Spectral Response for Long Wavelength Channel	17
4. Radiometer Relative System Spectral Response for Short Wavelength Channel	17
5. Schematic of Typical Radiometer Rocket Flight Characteristics	20
6. Ground Based Zenith Radiometer Measurement, Alaska, 21 March 1973	22
7. Ground Based Zenith Radiometer Measurement, Alaska, 6 April 1973	23
8. Ground Based Zenith Radiometer Measurement, WSMR, New Mexico, 3-4 October 1973	24
9. Ground Based Zenith Radiometer Measurement, WSMR, New Mexico, 3-4 October 1973	24
10. Measured TM Volts Versus Flight Time From 1.5642 μm on Rocket A30.205-5 (Alaska, 21 March 1973)	26
11. Measured TM Volts Versus Flight Time From 1.985 μm on Rocket A30.205-5 (Alaska, 21 March 1973)	26
12. Measured TM Volts Versus Flight Time From 1.5642 μm on Rocket A30.205-6 (Alaska, 6 April 1973)	27
13. Measured TM Volts Versus Flight Time From 1.985 μm on Rocket A30.205-6 (Alaska, 6 April 1973)	27
14. Measured TM Volts Versus Flight Time From 1.5642 μm on Rocket A030.311-2 (WSMR, New Mexico, 3 October 1973)	28
15. Measured TM Volts Versus Flight Time From 1.985 μm on Rocket A030.311-2 (WSMR, New Mexico, 3 October 1973)	28
16. Measured TM Volts Versus Flight Time From 1.5642 μm on Rocket A030.311-2 (WSMR, New Mexico, 3 October 1973)	29
17. Measured TM Volts Versus Flight Time From 1.986 μm on Rocket A030.311-3 (WSMR, New Mexico, 3 October 1973)	29
18. Altitude Profile of Radiance Measured on Rocket A30.205-5	33
19. Altitude Profile of Radiance Measured on Rocket A30.205-6	33
20. Altitude Profile of Radiance Measured on Rocket A030.311-2	34
21. Altitude Profile of Radiance Measured on Rocket A030.311-3	34
22. Ratio of Short to Long Wavelength Radiance Versus Altitude for Four Rocket Flights	37
23. Smoothed Radiance Data Measured on Rocket A030.311-3	40
24. Zenith Altitude Radiance Profiles Computed From Data Measured on Rocket A030.311-3	42
25. Volume Emission Rates Computed From Data Measured on Rocket A030.311-3	44

Illustrations

A1. Ortho-Normal Field of View (Rocket AO30.311-3)	50
A2. Ortho-Normal Field of View (Rocket AO30.311-3)	50
C1. Typical Magnetometer Calibration Data	62
C2. Magnetometer Geometry for Spinning Rocket in a Magnetic Field	63
C3. Schematic Showing Typical Magnetometer TM Volts Versus Flight Time	64
C4. Spherical Geometry of Coning Rocket	65

Tables

1. Summary of OH Rocket Launches	19
2. Radiometer Calibration Constants	31

Rocket Measurement of OH Emission Profiles in the 1.56 and 1.99 μ m Bands

1. INTRODUCTION

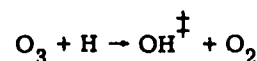
Under the sponsorship of the Defense Nuclear Agency several rocket measurement programs (ICECAP Programs) have been accomplished in the past few years to investigate infrared emissions in the upper atmosphere, particularly under disturbed conditions such as during aurora. Part of this effort has been dedicated to studies of emissions from the hydroxyl (OH) molecule using liquid nitrogen cooled radiometers onboard small rockets. Rocket measurements are employed in order to determine the altitude distributions of infrared emissions from which the mechanisms controlling the degree of OH excitation in the atmosphere are deduced. Results from the initial rocket experiment under the ICECAP program have been reported previously (Rogers et al¹). This report presents the results from five additional rocket measurements of OH emission profiles using similar payloads. Two of these payloads were flown from Poker Flat Rocket Range (PFRR), Alaska during the ICECAP 73 program (March, April 1973) and three were flown from White Sands Missile Range (WSMR), New Mexico in October 1973 during a joint Army/Air Force program called "Midlatitude Twilight D-Region Studies."

(Received for publication 23 January 1976)

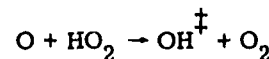
1. Rogers, J.W., Murphy, R.E., Stair, Jr., A.T., and Ulwick, J.C. (1973) Rocket-borne radiometric measurements of OH in the auroral zone, J. Geophys. Res. 78:7023.

The technique employed in these experiments was to measure the infrared emissions in the 1.56 and 1.99- μm bands with a dual channel radiometer payload as the rocket traversed the OH emitting layer (70 to 95 km). The bandpasses of the two channels were selected to encompass the 2-0 through 5-3, and the 7-5 through 9-7 OH vibration-rotation bands, respectively.

These particular optical bands were chosen in order to give information about the excitation processes responsible for the OH emissions. In particular the ozone process



can energetically excite up to and including the ninth vibrational level whereas other possible processes cannot excite as high levels. For example, the mechanism



can only excite $v = 6$ and lower levels. As a result, measurements of the emission in the two bands can give a relative measure of the completing mechanisms. This report documents the rocket data for these experiments and the data processing techniques used to determine the OH volume emission rates. In addition, some supporting measurements from ground-based instruments conducted during the rocket launches are presented.

2. INSTRUMENTATION

2.1 Rocket Payload Configuration

Determination of the altitude distribution of the OH emission can be accomplished by measurement of the integrated overhead infrared emissions through the altitude region from 70 to 95 km. The rocket/payload combination used for this purpose was a single-stage solid fuel Astrobe D equipped with cryogenically cooled dual-channel radiometers.

The rocket is a 6-in. diameter, fin-stabilized vehicle which provides adequate acceleration to offset surface wind effects, yet exhibits a relatively low sustained acceleration to minimize environmental problems. It is capable of carrying a payload weight of 30 lb to approximately 95 km in 140 sec (sea level conditions).

The primary sensor used for the OH measurements was a Utah State University dual-channel radiometer (Jensen et al²). A schematic of the radiometer is shown in Figure 1. It consists of an optical subsection containing Indium Antimonide (InSb) detectors, collecting optics, and interference filters in a cryogenic dewar cooled to near liquid nitrogen temperature (77°K). The components provide two independent optical channels, which utilize a common optical chopper to modulate the incident radiation. The system has an ejectable cold cover to keep the optical system cold and yet protect it from frosting until a suitable altitude (approximately 50 km) where the cover is ejected along with the payload nose tip, thereby exposing the radiometers (see Figure 2). The optical bandpass of each channel is determined by the interference filters, nominally $\lambda_0 = 1.5642$, $\Delta\lambda = 0.2057 \mu\text{m}$ for the low OH vibrational levels and $\lambda_0 = 1.9850$, $\Delta\lambda = 0.2027 \mu\text{m}$

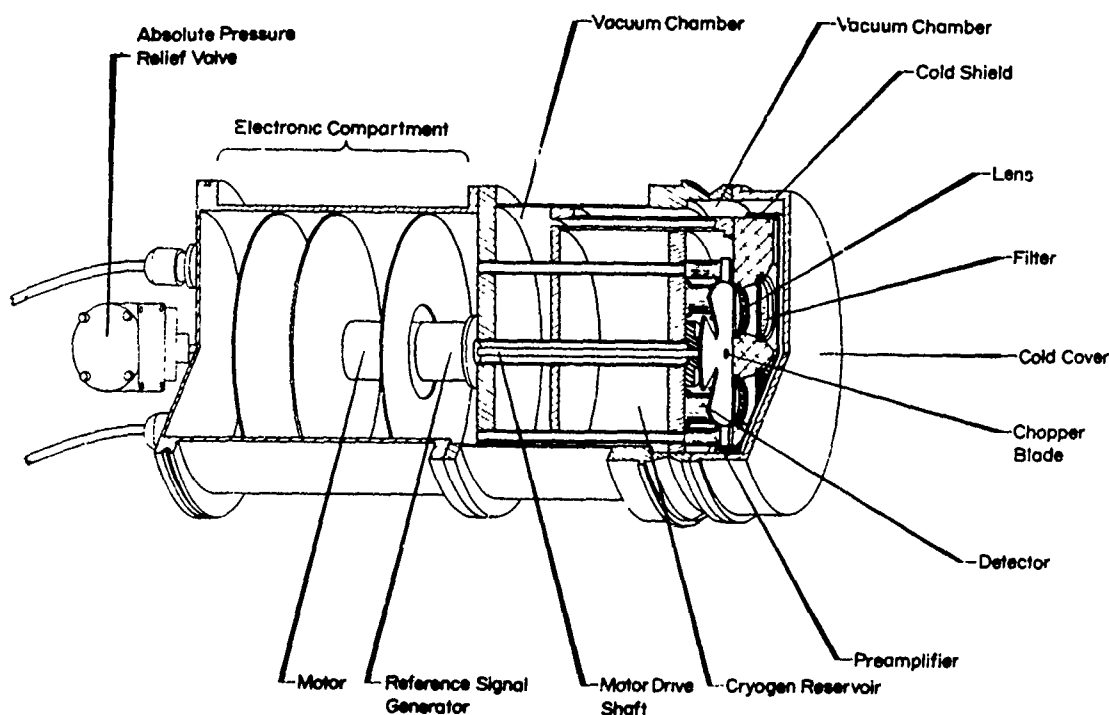


Figure 1. Schematic of Liquid Nitrogen Cooled OH Radiometer (Jensen et al²)

2. Jensen, L. L., Kemp, J. C., and Bell, R. J. (1972) Small Rocket Instrumentation for Measurement of Infrared Emissions, Astrobe D 30.205-3 and Astrobe D 30.205-4, Sci. Rept., No. 3, AFCRL 72-0691, Contract No. F19628-70-C-0302, Utah State University, Logan.

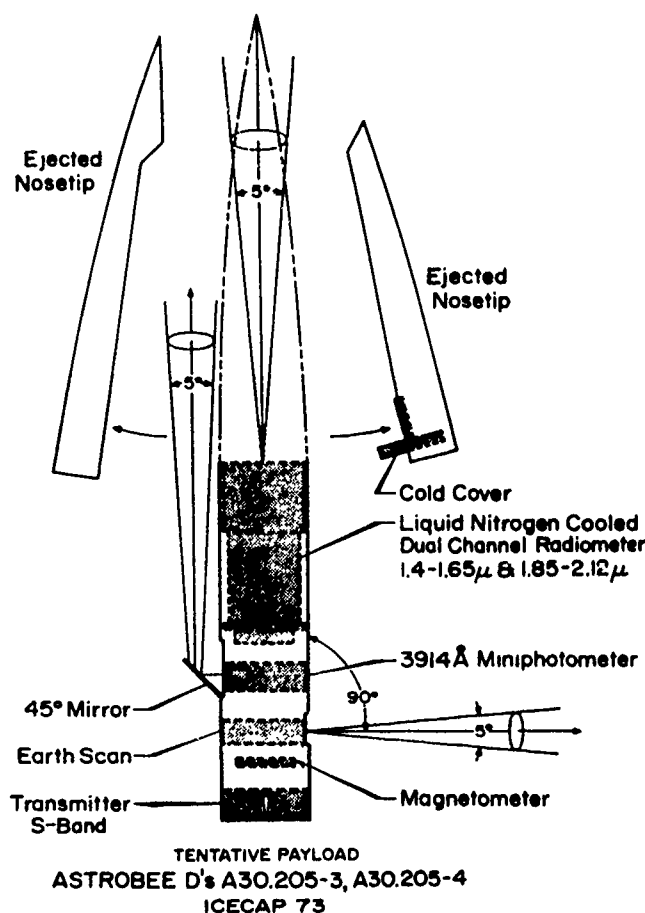


Figure 2. Astrobbee D Rocket Payload Configuration
Showing Nose Tip Ejection Technique and Nominal Fields
of View

for the high OH vibrational levels. The nominal system spectral response for each channel is shown in Figures 3 and 4 (Wyatt and Kemp³). A tabulation of the system spectral response data is included in Appendix A. The system wavelength passbands were computed by integrating the system spectral response and normalizing the result to an ideal filter of square response. For convenience, some references in this report to these passbands and center wavelengths will be shortened to $\Delta\lambda = 0.21 \mu\text{m}$ for the $\lambda_0 = 1.56\text{-}\mu\text{m}$ channel and $\Delta\lambda = 0.20 \mu\text{m}$ for the $1.99\text{-}\mu\text{m}$ channel.

3. Wyatt, C. L., and Kemp, J. C. () Calibration of SWIR Radiometers, Model NR-3B-8, NR-3B-9, NR-3B-10, NR-3B-11, NR-3B-12.

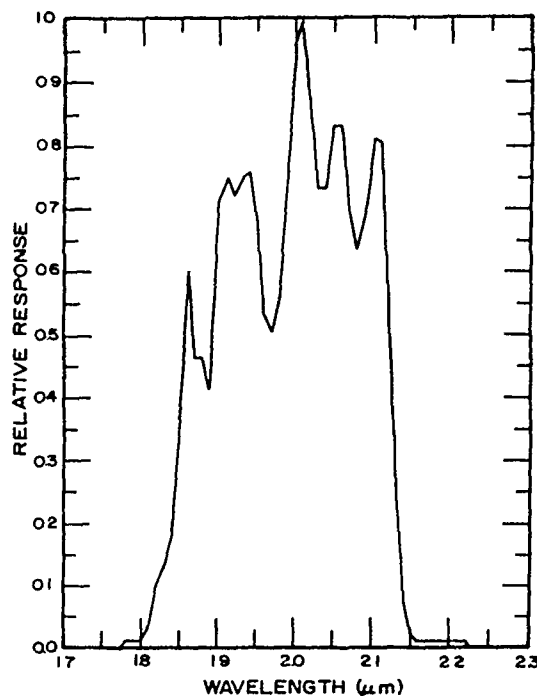


Figure 3. Radiometer Relative System Spectral Response for Long Wavelength Channel. Center wavelength $\lambda_0 = 1.985 \mu\text{m}$, equivalent spectral passband $\Delta\lambda = 0.2027 \mu\text{m}$)

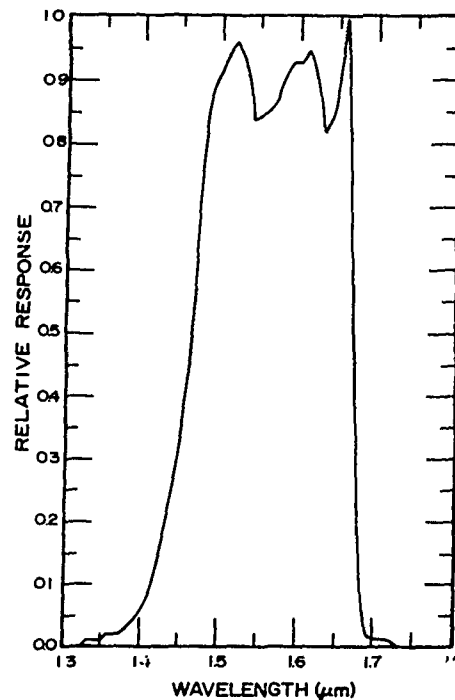


Figure 4. Radiometer Relative System Spectral Response for Short Wavelength Channel. Center wavelength $\lambda_0 = 1.5642 \mu\text{m}$, equivalent spectral passband $\Delta\lambda = 0.2057 \mu\text{m}$)

The radiometer optics consists of a simple $f/0.58$, high-transmission, coated, silicon lens and establishes the field-of-view of approximately 5° full angle (see Appendix A for measured fields of view). A light-emitting diode (LED) within the optical section is periodically activated to stimulate the detector and provide an inflight indication that the system is responding normally. Because of the variable nature of LED devices, the inflight radiometer signals resulting from them cannot be used for absolute calibration of the radiometer but serve only as a general indication of system performance. Special techniques were required to calibrate the radiometers and have been reported previously (Wyatt and Kemp³); however, the pertinent results of these calibrations are included in this report.

The electrical bandwidths of the radiometer channels are 1 Hz and consequently the instrument integration time is of the order of a second.

In addition to the radiometer, each payload was equipped with an aspect system consisting of a magnetometer (Schonstedt Instrument Company) and an infrared horizon sensor. For the auroral zone payloads, a photometer measuring N_2^+ emission at 3914A was also included to assess auroral conditions prevailing during the

OH measurements. Temperature sensors were included in all payloads to monitor the environment in critical areas of the payload and to assess instrument performance.

Standard frequency deviation multiplexing telemetry (FM/FM) techniques were used to transmit the sensor data to the ground. The analog voltage signals (0 to +5V) from the rocket sensors were used to frequency modulate standard IRIG subcarrier oscillators (IRIG channels 12 through 16) — each data output was assigned a separate subcarrier frequency. The modulated subcarriers were then multiplexed into a single composite signal which was used to frequency modulate an S-band telemetry transmitter. The ground telemetry stations received the S-band carrier and detected the FM composite signal containing the measured information. The composite signal was direct recorded on magnetic tape at 60 in. per second along with IRIG B format Universal Time Code. The recorded single composite signal containing the data from all the sensors on the rocket is the starting point for processing to retrieve the measured information.

2.2 Ground-Based Instrumentation

A variety of ground-based optical/infrared and ionospheric sounding instrumentation was operated in support of the rocket programs both at PFRR and WSMR. At both locations, the AFCRL Mobilab and the Utah State University Mobile Observatory (ARGUS) were operated. Instrumentation in these facilities included interferometer-spectrometers, photometers (fixed and spatially scanning), all sky cameras, 30-MHz riometer and several near-infrared radiometers. At PFRR, the University of Alaska provided additional optical support as well as magnetometer coverage. A complete description of these systems and interpretation of results obtained is beyond the scope of this report; however, some data are included in the text where relevant to define the geophysical conditions prevailing during the rocket flights.

3. ROCKET FLIGHT SUMMARY

Table 1 summarizes the rocket flights flown during the OH measurement programs at PFRR and WSMR. Other rocket experiments were also conducted during these field programs, but are not reported here.

3.1 Rocket Flight Characteristics

An understanding of rocket flight characteristics, particularly the instrument viewing aspect, is critical to correct interpretation of the infrared measurements. Of particular importance is the increase in signal commonly referred to as

Table 1. Summary of OH Rocket Launches

Launch Site ⁽¹⁾	Rocket Number	Launch Data/Time ⁽²⁾ (UT)	Launch Conditions
PFRR	A30.205-5	080.1011:00.000 (21 Mar 1973)	Nighttime Normal OH Background
PFRR	A30.205-6	096.0845:00.000 (6 April 1973)	Nighttime Quiet OH Background
WSMR	AO30.311-1	276.0040:00.949 (4 Oct 1973)	Sunset
WSMR	AO30.311-2	276.0127:00.818 (4 Oct 1973)	Twilight OH
WSMR	AO30.311-3	276.0500:00.716 (4 Oct 1973)	Nighttime Quiet OH

Rocket Number	Solar Zenith Angle (deg)	Apogee (km)	Altitudes of Usable Data (km)
A30.205-5	114.7	78	55-78 Ascent 78-25 Descent
A30.205-6	107.5	78	53-78 Ascent
AO30.311-1	56	52 ⁽³⁾	None ⁽³⁾
AO30.311-2	99	102	52-78 Ascent
AO30.311-3	141	106	55-106 Ascent 106-74 Descent

(1) PFRR - Poker Flat Rocket Range, Alaska; WSMR - White Sands Missile Range, New Mexico.

(2) Date/Time - Julian day hours, minutes: seconds. milliseconds UT.

(3) Early tip ejection resulted in loss of data.

van Rhijn effect (Chamberlain⁴), when an emitting region is viewed obliquely rather than vertically. The optical axis of the radiometer was aligned with the rocket axis in each case so that any inclination of the rocket with respect to the vertical, allows the radiometer to view a greater optical path through an emitting layer resulting in a larger measured signal.

4. Chamberlain, J.W. (1961) Physics of the Aurora and Airglow, Academic Press, New York and London.

A scenario of a typical Astrobe D rocket flight is illustrated in Figure 5. The rocket is launched at an elevation angle of about 85° . At about 20 sec after liftoff, the motor propellant burns out. At this time, the rocket has attained a spin rate of about 8 rps due to the effect of the rocket fins. In addition to the rocket spin (roll), the vehicle usually exhibits a coning (precession) motion with a period considerably longer than the spin period, typically 20 to 30 sec. When the rocket has achieved an altitude of about 55 km, the atmospheric drag is small and the vehicle is essentially in free ballistic flight, allowing the payload tip to be safely ejected permitting the radiometers to view the incident infrared radiation. The ejection of the tip usually aggravates the coning motion. The vehicle continues this motion through apogee and for a time on descent while the vehicle is falling tail first. Finally, around 70 km, the effect of atmospheric drag perturbs the vehicle motion: it begins to tip over, oscillates for a time, and then reenters nose first. Thus, radiometer airglow measurements are possible from tip ejection (55 km) to vehicle tip over (~ 70 km) when the instruments view the earth.

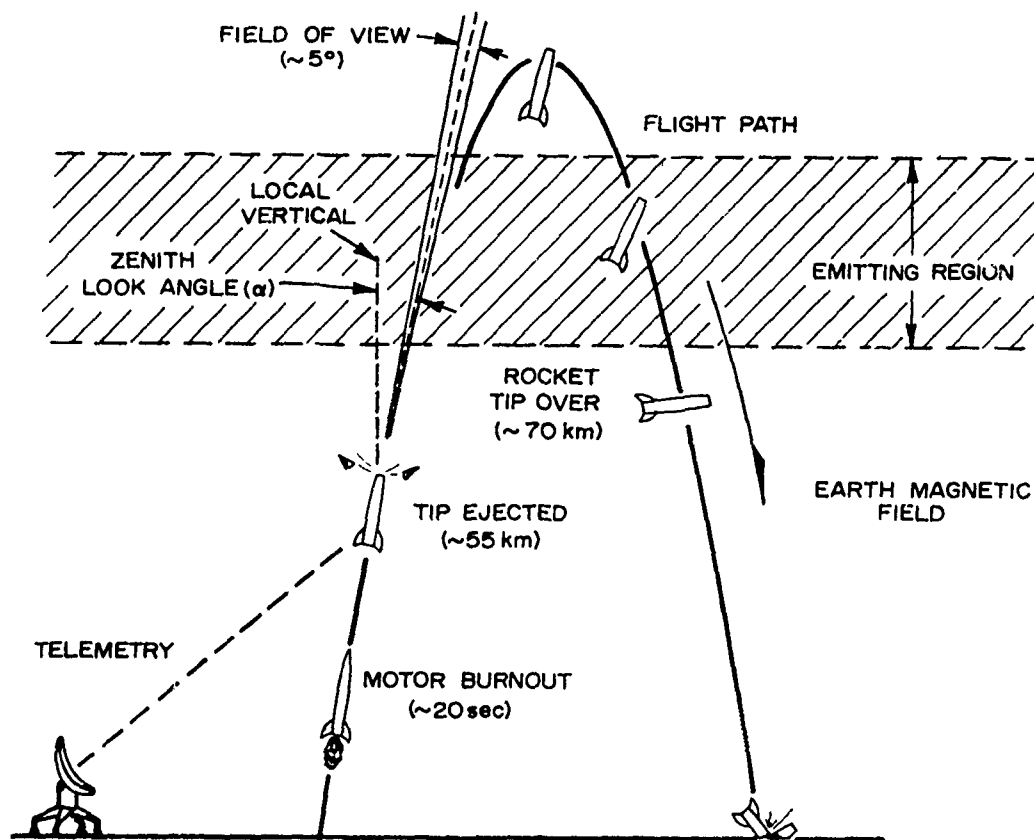


Figure 5. Schematic of Typical Radiometer Rocket Flight Characteristics

3.2 Launch Conditions and Payload Performance

The two OH rockets flown at PFRR in March and April 1973 (A30.205-5 and A30.205-6) underperformed and achieved apogee altitudes less than expected. However, good data were measured from tip-eject altitude to apogee and during descent as indicated in Table 1. Supporting ground-based radiometric measurements accomplished during the night of 21 March 1973 indicated a generally normal auroral zone OH background of approximately 200 kilorayleighs in the wavelength region $\lambda_0 = 1.573 \mu\text{m}$ and $\Delta\lambda = 0.212 \mu\text{m}$ at the time of rocket A30.205-5 flight (see Figure 6) (Huppi,⁵ personal communication). Some auroral activity had been present earlier in the evening. During the night of 6 April 1973 (A30.205-6) clouds interfered with the ground measurements (see Figure 7), but at the time of rocket launch there were enough breaks in the cloud cover to ascertain that the OH level (in the same spectral band mentioned above) was reasonably quiet (Huppi⁵ [personal communication] estimates a level of the order 150 kilorayleighs). During both flights, the onboard 3914-A photometers indicate stable low levels near the minimum detectable of the instruments ($\sim 200 \text{ R}$).

The three rockets flown at WSMR were timed to study altitude profiles of OH emissions associated with twilight-night transition phenomena. Figures 8 and 9 show the OH levels measured from the ground (Huppi,⁵ personal communication) during the night of the rocket flights with radiometers in the bandpasses $\lambda_0 = 1.683$, $\Delta\lambda = 0.071$ and $\lambda_0 = 1.573$, $\Delta\lambda = 0.212$ micrometers. Also indicated on the figures are the times of rocket launches relative to the OH levels.

Rocket AO30.311-1 was launched prior to sunset (solar zenith angle was approximately 86 degrees). Due to early tip ejection, this rocket underperformed and the flight instrument heated up resulting in a loss of all mesospheric data. The second rocket (AO30.311-2) was launched at the time of minimum OH emission when the OH level was approximately 40 kilorayleighs in the $1.683\text{-}\mu\text{m}$ band and 200 kilorayleighs in the $1.573\text{-}\mu\text{m}$ band (see Figures 8 and 9). The solar zenith angle was about 99° at this time. The rocket performed satisfactorily and data were obtained from tip ejection altitude to 78 km where direct sunlight on the instrument prohibited measurements.

A slight enhancement in the OH level (ground based radiometer $1.683\text{-}\mu\text{m}$ channel) began at approximately 0130 UT and peaked at a level of about 55 kilorayleighs at 0220 UT. This enhancement is typical of the transition period and is also discernable in the $1.573\text{-}\mu\text{m}$ channel. The third rocket (AO30.311-3) was launched at 0500 UT when the OH level was dropping (44 kilorayleighs in the $1.683\text{-}\mu\text{m}$ band and 190 kilorayleighs in the $1.573\text{-}\mu\text{m}$ band). This rocket and payload performed

5. Huppi, R.J. (1973) Private communication.

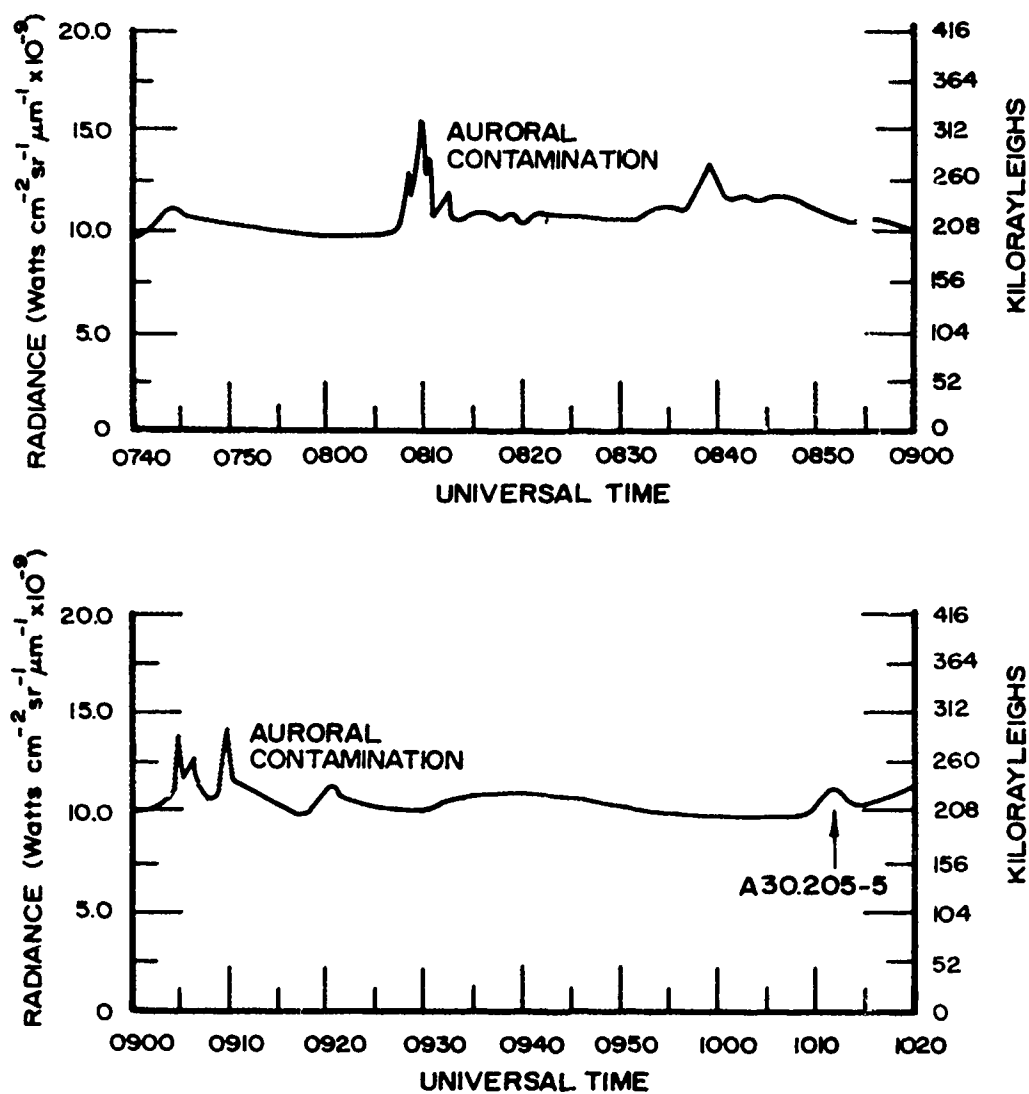


Figure 6. Ground Based Zenith Radiometer Measurement, Poker Flat, Alaska, 21 March 1973 (UT). $\lambda_0 = 1.573 \mu\text{m}$, $\Delta\lambda = 0.212 \mu\text{m}$, F.O.V. = 2.8° (Huppi⁵)

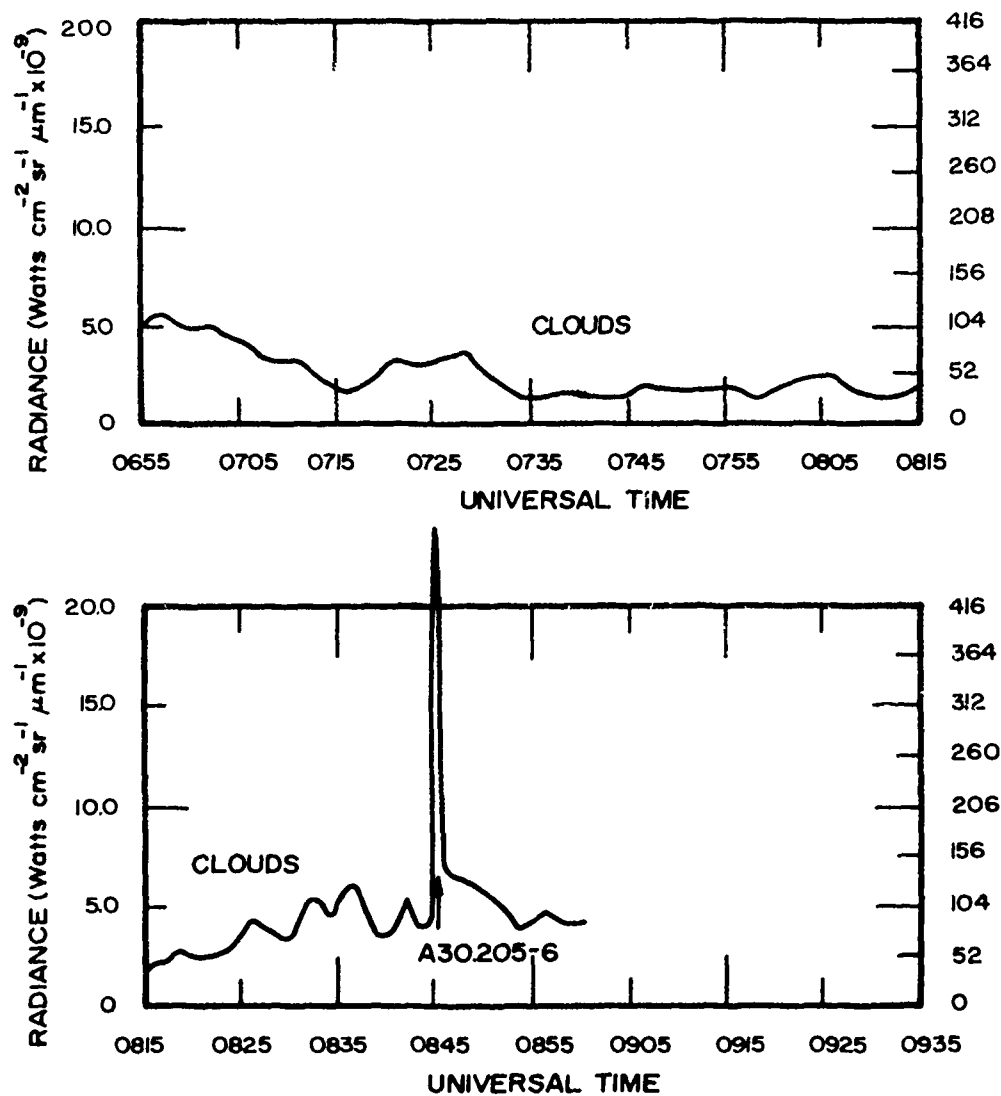


Figure 7. Ground Based Zenith Radiometer Measurement, Poker, Alaska, 6 April 1973 (UT). $\lambda_c = 1.573 \mu\text{m}$, $\Delta\lambda = 0.212 \mu\text{m}$, F.O.V. = 2.8° (Huppi⁵). Launch of rocket A30.205-6 is indicated at 0845 UT

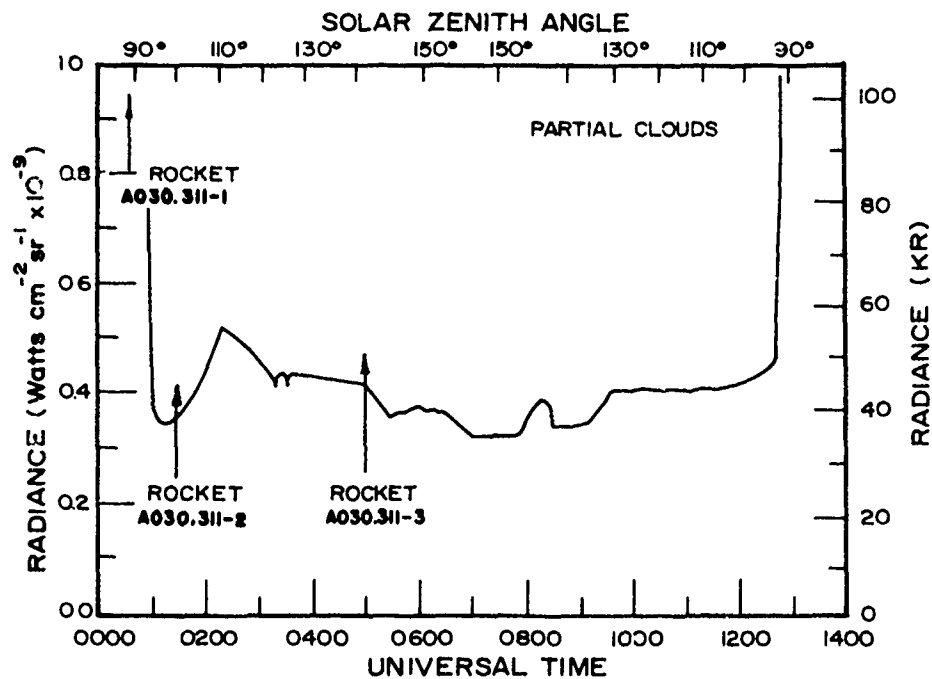


Figure 8. Ground Based Zenith Radiometer Measurement, WSMR, New Mexico, 3-4 October 1973 (UT). $\lambda_o = 1.683 \mu\text{m}$, $\Delta\lambda = 0.07 \mu\text{m}$, F.O.V. = 2.8° (Huppi⁵)

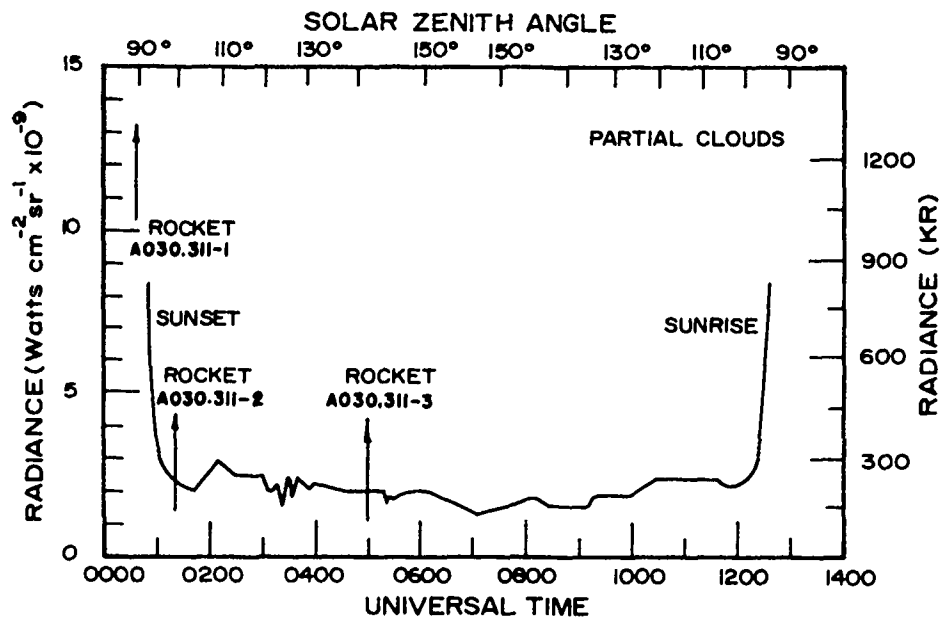


Figure 9. Ground Based Zenith Radiometer Measurement, WSMR, New Mexico, 3-4 October 1973 (UT). $\lambda_o = 1.573 \mu\text{m}$, $\Delta\lambda = 0.212 \mu\text{m}$, F.O.V. = 2.8° (Huppi⁵)

minimally and good data were obtained from 54 km through apogee (106 km) and during descent to 74 km where the rocket tipped over and reentered.

Ground based riometer (30 MHz) data taken during the period 2 October through 4 October 1973 at WSMR indicated that no detectable ionospheric absorption events occurred preceding or during the rocket flights.

4. ROCKET DATA PROCESSING

4.1 Digitization of Data

The recorded composite telemetry signal for each flight was discriminated to separate individual sensor channels and reduce the frequency modulated subcarrier data to analog output voltages. Each voltage output was digitized at a rate of 1660 points/sec, correlated with time after launch and coded in a format compatible with the AFCRL CDC 6600 digital computer. This computer was used for all data processing and plotting.

Figures 10 through 17 show the computer plots of telemetered sensor volts for each of the radiometer channels (denoted by IRIG channel) on each rocket as a function of time after launch in seconds. These represent the fundamental data from which all further processing was accomplished.

In general, the data for each of the rocket flights are similar. Prior to the nose tip ejection (approximately 50 sec) the radiometers view the cold cover and the voltage is near zero (explanation of the slightly negative voltages in some channels will be discussed later). After the tip (and cold cover) are ejected, the instruments view the emitting region above and the voltage levels show a marked increase. The initial large scale modulation of data thereafter is due to coning of the rocket which produces the van Rhijn enhancement. The periodic spikes in the data labeled "inflight calibration" result from activation of the light emitting diode for systems check.

Referring to Figures 16 and 17, after a period of modulated high voltage levels, the signal decays to near zero because the rocket (radiometer) has passed through the emission region. The low signal remains through apogee (around 140 sec) and then increases again as the rocket descends (tail first) through the emitting regions once more (see Figure 5). After 220 sec, the rocket has descended to a low enough altitude where the fins are affected by air drag and the rocket tips over. During this period, the radiometers view first the horizon and then the earth. Once the rocket tips over and begins reentry, the radiometer optics become warm and saturate both channels.

The absence of any marked signal decay after tip ejection in Figures 10, 11, 12 and 13 indicates that these rockets did not pass through the main layer of OH

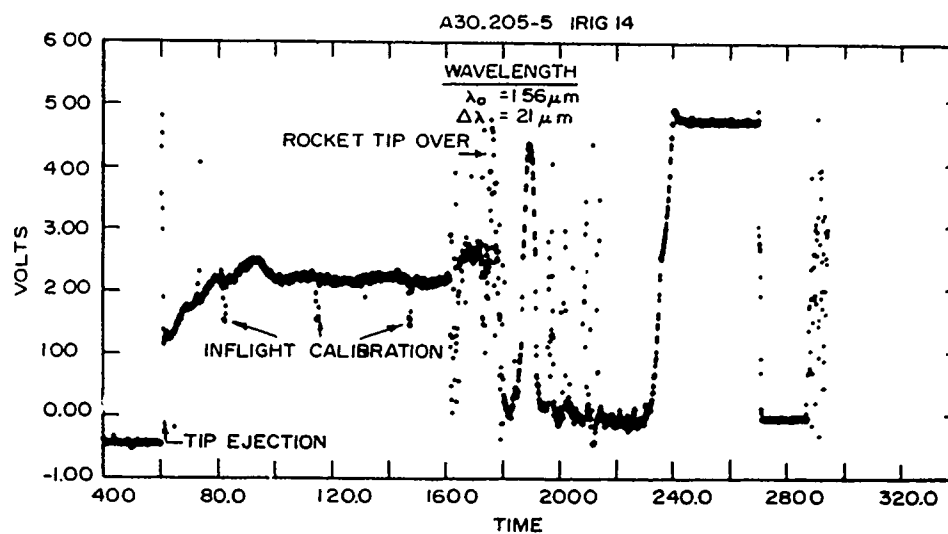


Figure 10. Measured Telemetry Volts Versus Flight Time in Seconds From 1.5642- μm Rocket Radiometer Channel. Rocket A30.205-5 Poker Flat, Alaska, 21 March 1973 (UT)

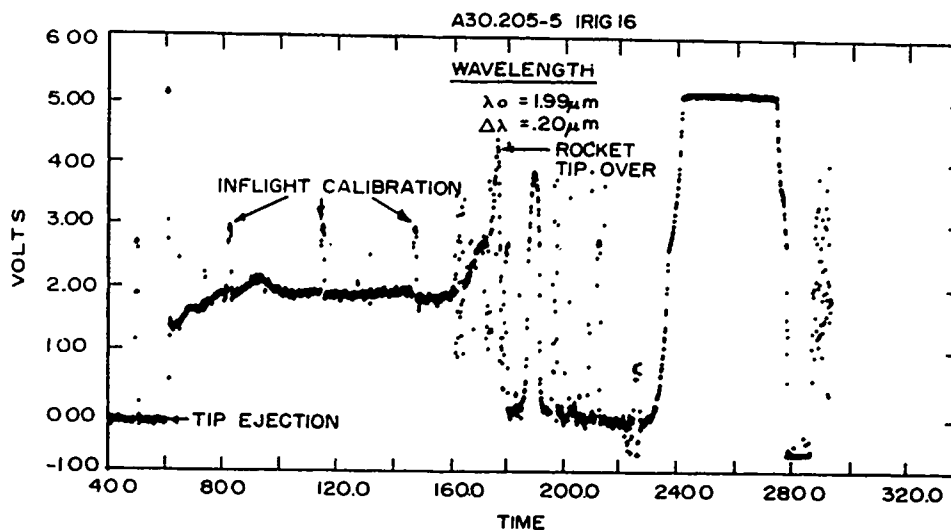


Figure 11. Measured Telemetry Volts Versus Flight Time in Seconds From 1.985- μm Rocket Radiometer Channel. Rocket A30.205-5, Poker Flat, Alaska, 21 March 1973 (UT)

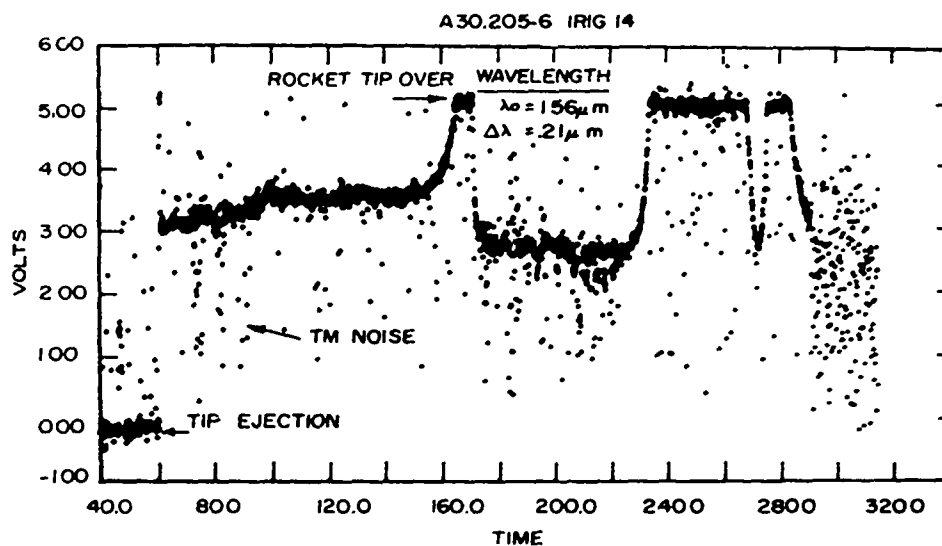


Figure 12. Measured Telemetry Volts Versus Flight Time in Seconds From 1.5642- μm Rocket Radiometer Channel. Rocket A30.205-5, Poker Flat, Alaska, 6 April 1973 (UT)

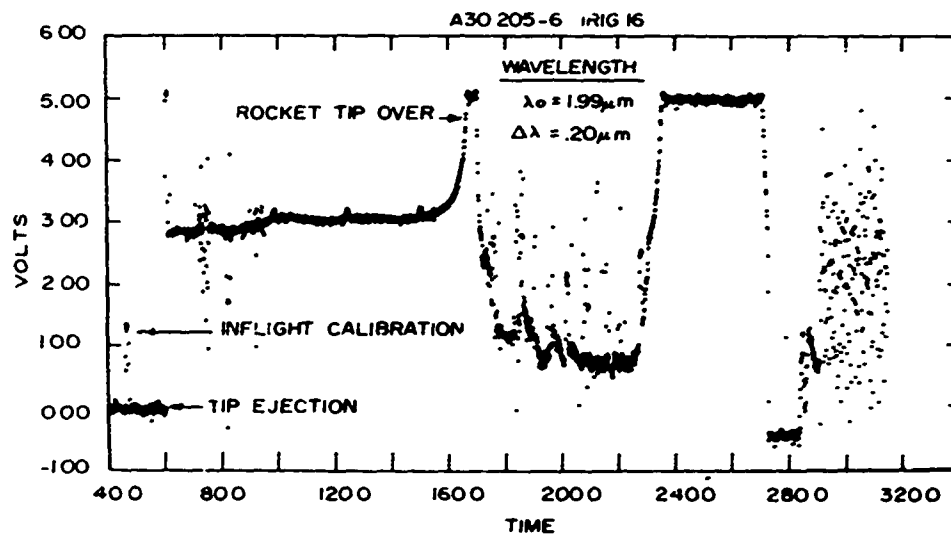


Figure 13. Measured Telemetry Volts Versus Flight Time in Seconds From 1.985- μm Rocket Radiometer Channel. Rocket A30.205-6, Poker Flat, Alaska, 6 April 1973 (UT)

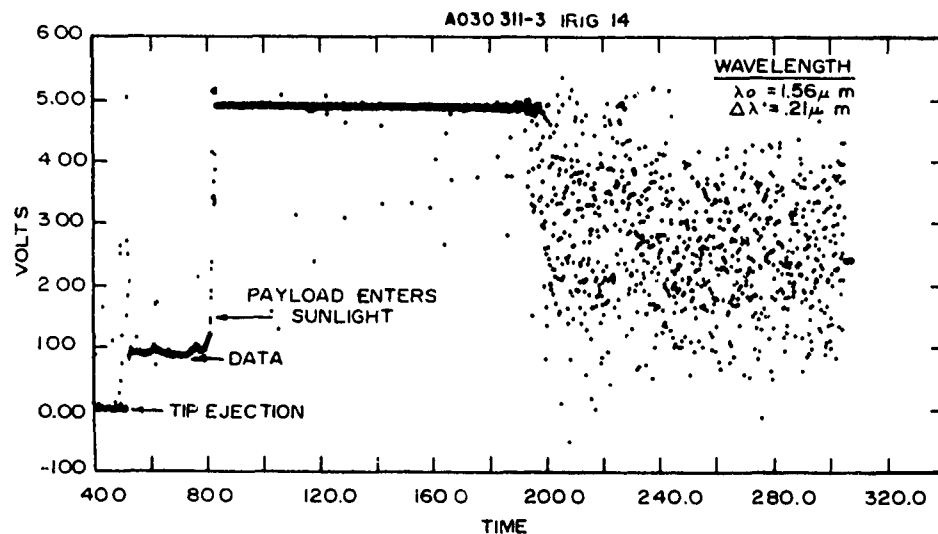


Figure 14. Measured Telemetry Volts Versus Flight Time in Seconds From 1.5642- μm Rocket Radiometer Channel. Rocket A030.311-2, WSMR, New Mexico, 3 October 1973 (UT)

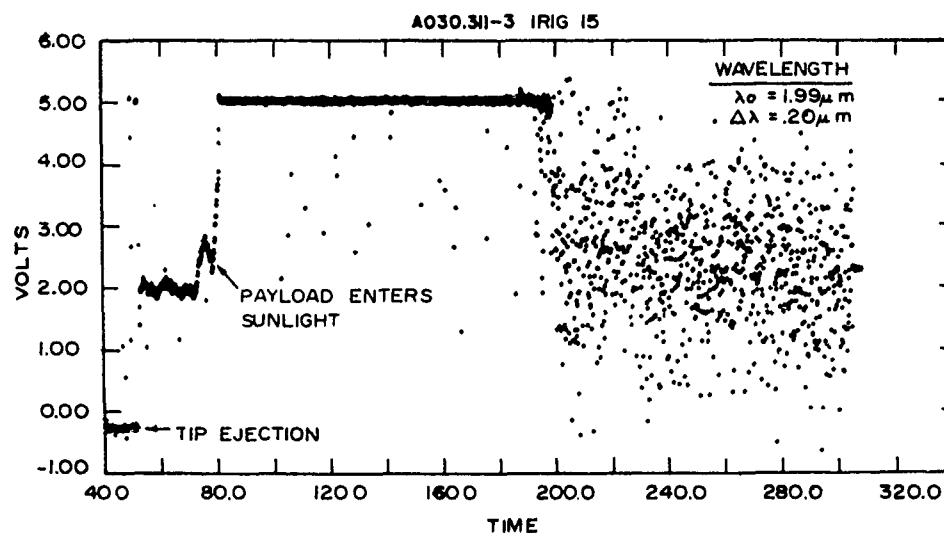


Figure 15. Measured Telemetry Volts Versus Flight Time in Seconds From 1.985- μm Rocket Radiometer Channel. Rocket A030.311-2, WSMR, New Mexico, 3 October 1973 (UT)

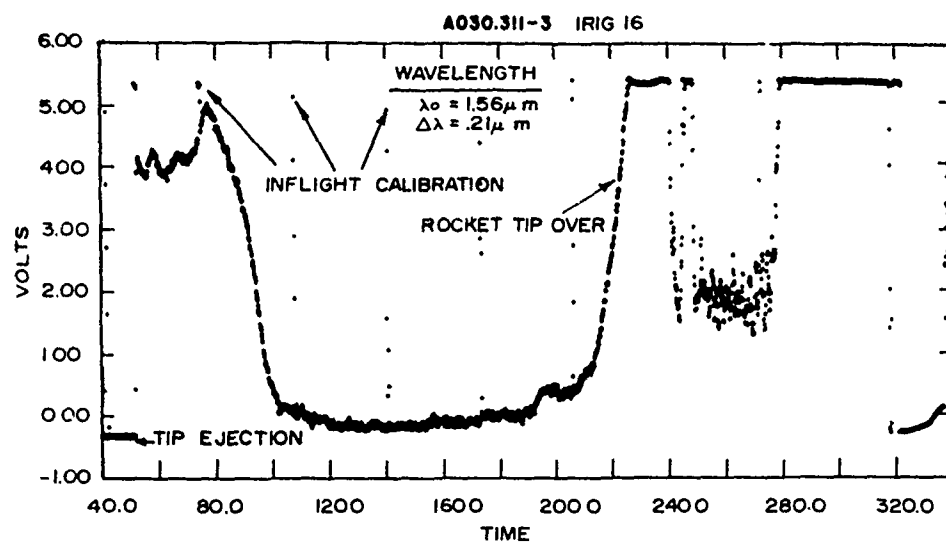


Figure 16. Measured Telemetry Volts Versus Flight Time in Seconds From 1.5642- μm Rocket Radiometer Channel. Rocket AO30.311-3, WSMR, New Mexico, 3 October 1973 (UT)

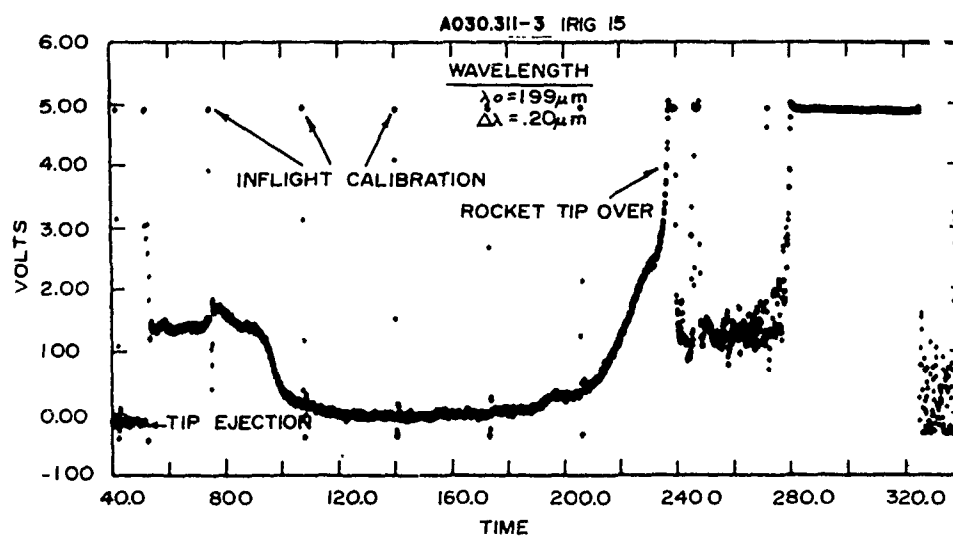


Figure 17. Measured Telemetry Volts Versus Flight Time in Seconds From 1.986- μm Rocket Radiometer Channel. Rocket AO30.311-3, WSMR, New Mexico, 3 October 1973 (UT)

emissions. In Figures 14 and 15, the appearance of signal saturation around 70 sec was caused by the incidence of solar radiation on the instrument as discussed previously.

The fine structure in all the data is attributed to instrument, telemetry and recording system noise rather than rocket spin since the instrument inherent long integration time is much longer than the rocket spin period.

4.2 Measured Altitude Emission Profiles

The voltage-time data in Figures 10 through 17 were converted to kilorayleigh radiance profiles using trajectory data and the following calibration equation:

$$R_{\alpha} = rV + C \quad (1)$$

where

R_{α} = radiance measured at zenith angle α (kilorayleighs)

r = inverse responsivity (kilorayleighs/volt)

V = telemetry signal (volts)

C = instrument offset constant (kilorayleigh)

The radiance (L_{α}) in watts-cm⁻²-ster⁻¹ can be approximated using the following relationship (Baker⁶):

$$L_{\alpha} = \frac{R_{\alpha}}{2\pi\lambda_0} \times 10^{-10} \quad (2)$$

where

$\lambda_0 = 1.9850 \mu\text{m}$ for the high wavelength channel and $\lambda_0 = 1.5642 \mu\text{m}$ for the low wavelength channel.

The appropriate constants used in Eq. (1) for each radiometer channel are given in Table 2 (Wyatt et al³). The offset constant (C) is a feature of the differential amplifiers in the radiometer electronics. The drift of this offset is a common problem with DC amplifiers unless elaborate means are used to compensate for it. However, as long as the product rV is large compared to C in Eq. (1), errors in computing radiance caused by drift in C are minimal. For this reason the high gain channels (characterized by highest voltages) as opposed to low gain channels, were used where possible in reducing the radiometer data. In all cases, the offset

6. Baker, D.J. (1974) Rayleigh, the unit of light radiance, Applied Optics 13:2160.

Table 2. Radiometer Calibration Constants

Rocket Number	IRIG	λ_o Center Wavelength (microns)	Voltage Limits (volts)
A30.205-5	16	1.985	$-.20 < V < 2.71$ $2.71 < V < 5.0$
	14	1.5624	$-.45 < V < 2.64$ $2.64 < V < 4.80$
A30.205-6	16	1.985	$-.20 < V < 2.725$ $2.725 < V < 4.85$
	14	1.5642	$-.15 < V < 2.724$ $2.724 < V < 5.0$
AO30.311-2	15	1.985	$0 < V < 5.0$
	14	1.5642	$0 < V < 5.0$
AO30.311-3	15	1.985	$-.20 < V < 5.5$
	16	1.5642	$-.35 < V < 5.5$

Rocket Number	N Inverse Responsibility (kilorayleighs/volt)	C Offset Constant (kilorayleighs)
A30.205-5	56.86 627.24	+11.37 -1546.28
	70.86 828.5	+30.47 -1985.3
A30.205-6	57.24 508.78	+1.14 -1222.1
	36.86 413.76	+5.52 -1031.9
AO30.311-2	24.19 216.43	+7.48 -9.93
	68.59 34.79	12.4 +12.18

calibration constants were adjusted to agree with the voltage level measured just prior to tip ejection.

Radiance plots of the data as a function of rocket altitude are shown in Figures 18, 19, 20 and 21 for each of the rockets (in-flight calibrations, pre tip-ejection data, and obvious spurious noise have been omitted for clarity). Magnetometer pitch angle data (explained in the next paragraph) are also shown on these plots.

4.3 Magnetometer Aspect Data Reduction

Each rocket payload contained a magnetic aspect sensor (magnetometers) oriented with its sensing axis perpendicular to the rocket axis (see Figure 2). The rocket magnetometer data alone can provide only rocket cone angle, axis of precession relative to the earth's magnetic field and spin and precession rates. Although it is not possible to completely define rocket aspect with magnetometer data alone, a reasonable approximation can be made in cases where "well behaved" flight motion can be assumed (Marcou⁷) and additional aspect parameters are available, such as knowledge of the functional variation of other measured data with aspect. The measured OH emission altitude profiles, for instance, provide some insight into rocket aspect, viz., van Rhijn effect.

The basic equations relating magnetometer output voltage and aspect parameters are derived in Appendix C. The pertinent equations are repeated here in order to explain the data processing employed.

The instantaneous magnetometer output voltage is related to both the angle between the earth's magnetic field and the sensing axis of the magnetometer and the rocket spin frequency by

$$v = v_{ave} + \frac{B_o}{k} \sin \gamma \cos \omega_s t \quad (3)$$

where

v = instantaneous voltage output from the magnetometer

γ = angle between earth's magnetic field vector and rocket axis

ω_s = rocket spin radian frequency

B_o = total intensity of the earth's magnetic field (milligauss)

k = magnetometer calibration factor (milligauss/volt)

7. Marcou, R. J., and Sullivan, B. J. (1967) Aspects for a Rocket From Magnetometer Data, AFCRL 67-0424, Air Force Cambridge Research Laboratories, Bedford.

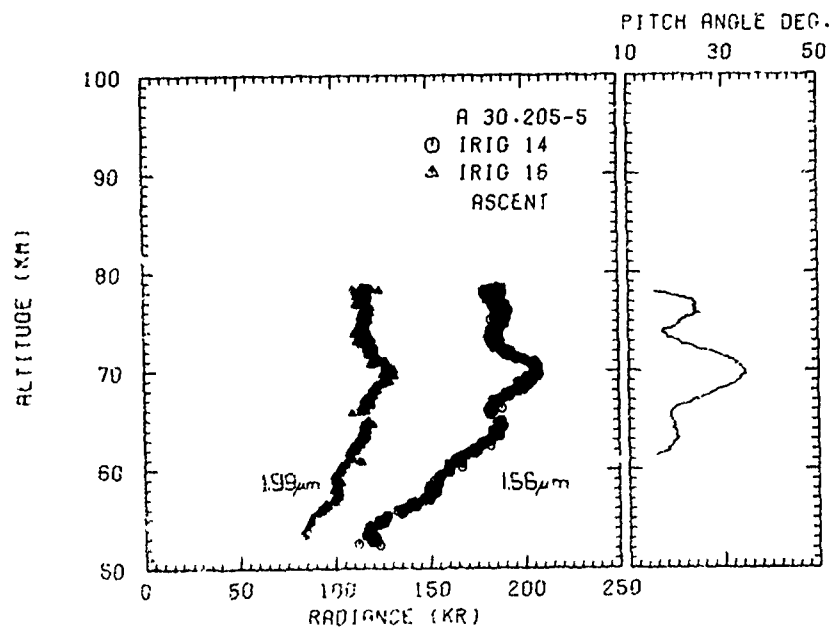


Figure 18. Altitude Profile of Radiance (kilorayleighs) in the $\lambda_o = 1.5642 \mu\text{m}$ (IRIG 14) and $\lambda_o = 1.985 \mu\text{m}$ (IRIG 16) Bands, Rocket A30.205-5. Data not corrected for rocket aspect

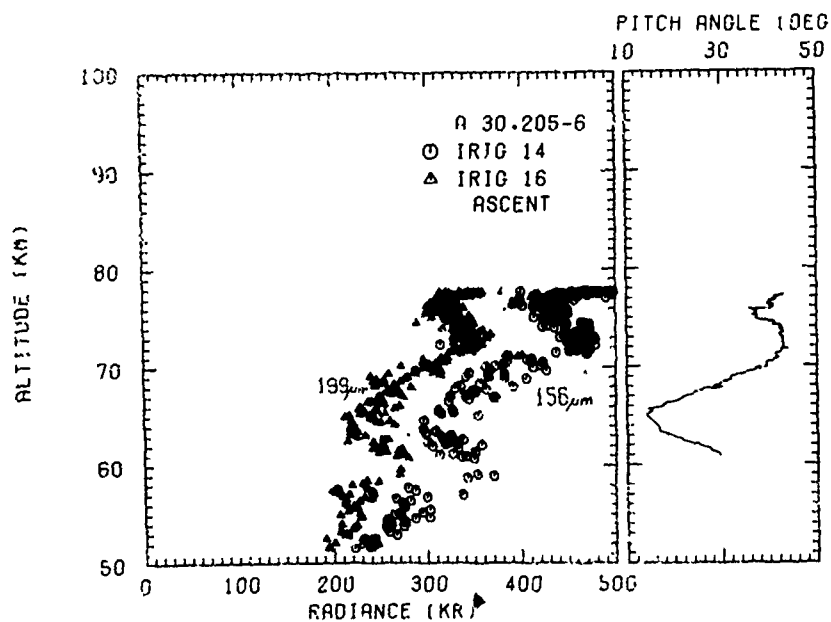


Figure 19. Altitude Profile of Radiance (kilorayleighs) in the $\lambda_o = 1.5642 \mu\text{m}$ (IRIG 14) and $\lambda_o = 1.985 \mu\text{m}$ (IRIG 16) Bands, Rocket A30.205-6. Data not corrected for rocket aspect

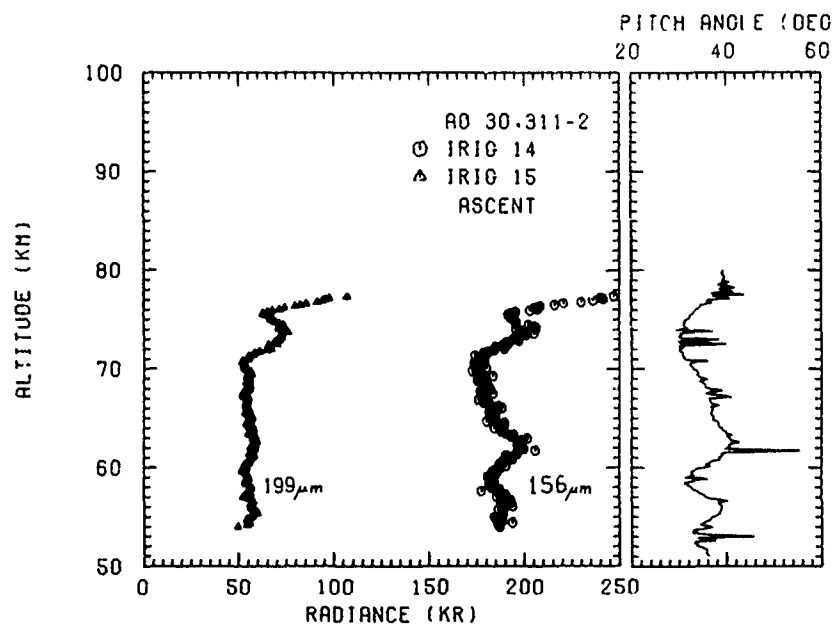


Figure 20. Altitude Profile of Radiance (kilorayleighs) in the $\lambda_0 = 1.5642 \mu\text{m}$ (IRIG 14) and $\lambda_0 = 1.985 \mu\text{m}$ (IRIG 15) Bands, Rocket AO30.311-2. Data not corrected for rocket aspect

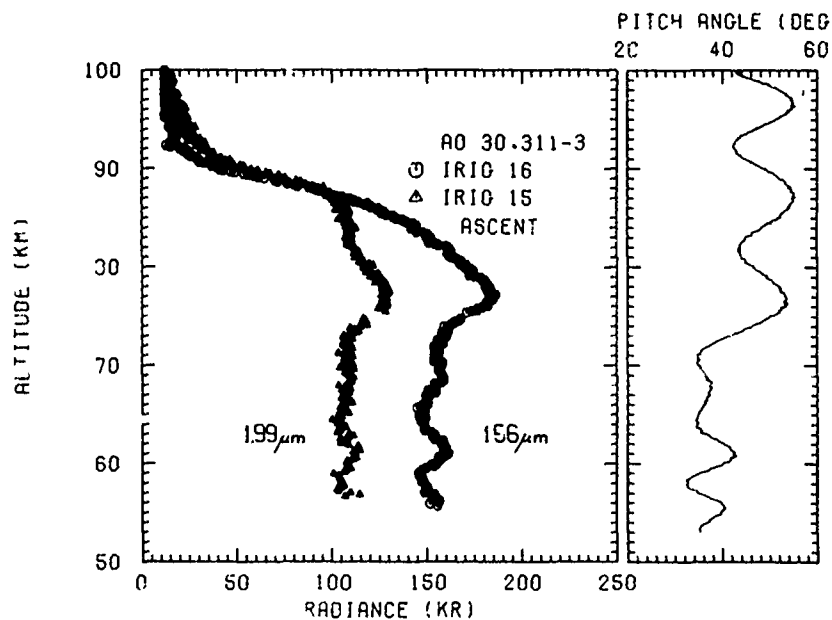


Figure 21. Altitude Profile of Radiance (kilorayleighs) in the $\lambda_0 = 1.5642 \mu\text{m}$ (IRIG 16) and $\lambda_0 = 1.985 \mu\text{m}$ (IRIG 15) Bands, Rocket AO30.311-3. Data not corrected for rocket aspect

t = flight time (seconds)

v_{ave} = average magnetometer output voltage.

Equation (3) is an amplitude modulated waveform where the carrier frequency is ω_s (due to rocket spin) and the amplitude modulating function is $\sin \gamma$ (due to rocket coning). As shown in Appendix C, as long as γ varies slowly compared to the spin ω_s then (see Figure C3)

$$\sin \gamma = \frac{k}{B_0} (v_u - v_{ave}) \quad (4)$$

where

v_u = upper instantaneous envelope voltage from the magnetometer.

The first step in reducing the magnetometer data was to evaluate the average envelope voltage (v_{ave}) from the measured data. This was computed by simply averaging the instantaneous maximum (upper envelope) and minimum (lower envelope) output voltage from the magnetometer data as a function of flight time. The value of v_{ave} was found to be reasonably constant for a particular rocket flight. With the value of v_{ave} established, γ was computed as a function of flight time using Eq. (4). The value of the calibration constant k was supplied by the manufacturer ($k = 250$ milligauss/volt) and the value of the earth's local magnetic field intensity (B_0) at ground level was used for rockets flown at each launch site (for WSMR, $B_0 = 500$ milligauss and for PFRR $B_0 = 560$ milligauss). Plots of pitch angle, defined as $180^\circ - \gamma$, for each rocket as a function of rocket altitude are shown in Figures 18, 19, 20 and 21. These data represent the basic information from which rocket aspect relative to local vertical (zenith angle) is deduced in the discussion section of this report. The magnetometer data from rockets A30.205-5 and 6 was multiplexed with horizon sensor data causing degraded magnetometer records that could not be processed with standard computer techniques. The data shown in Figures 18 and 19 for these rockets were manually reduced.

In considering the magnetometer data presented, it is important to understand that the pitch angle as computed represents a cone about the magnetic field vector on which the rocket axis can lie. Any position on this cone will produce the same magnetometer output voltage. For this reason it is essential to introduce additional evidence and/or assumptions to deduce the rocket position on the locus cone.

5. DISCUSSION

5.1 Intensity Ratio Profiles

From an inspection of the measured emission profiles shown in Figures 18, 19, 20 and 21, it is clearly evident that the data are significantly modulated by the rocket coning motion. In general, this can be attributed to a van Rhijn effect (Peterson⁸) if the emissions are assumed to emanate from a homogeneous optically thin layer. The effects of aspect must be accounted for if absolute values of intensity are to be compared between rockets. This is usually accomplished by correcting all data to zenith profiles using a van Rhijn factor, viz.

$$R_o = \frac{R_\alpha}{V_\alpha} \quad (5)$$

where

R_o = zenith radiance at altitude h

R_α = radiance measured at an angle α from the vertical at an altitude h

V_α = van Rhijn factor for angle α at an altitude h .

For the two channel radiometer systems used in these measurements, it can be assumed that the van Rhijn factors are the same for each channel on any one rocket because both have the same aspect at any instant in time and the measured emissions emanate from about the same altitude (Rogers et al¹). Thus, the ratio of measured intensities from the two channels on any one rocket is the same as the ratio of the zenith emissions. Consequently, the ratios of the two wavelength channels from each rocket measurement can be compared with the ratios measured with the other rockets. The ratio of the short wavelength channel (1.5642 μm) to the long wavelength channel (1.985 μm) on each rocket were computed and plotted as a function of altitude (see Figure 22).

Considering first the ratio data shown in Figure 22 for emission intensities measured on rocket AO30.311-3 (midlatitude nighttime flight), there is clearly little effect of aspect compared to the aspect modulation on the individual channel intensity data in Figure 21. The data for this rocket show a nearly constant ratio value of about 1.4 up to 83 km. As the rocket penetrates the main layer of emission (above 83 km), the ratio diminishes to a value of about 0.5 at 93 km. At 92.5 km, the measured long and short wavelength intensities are equal as the ratio is 1. The

8. Peterson, A.W., and Kieffaber, L.M. (1972) Airglow fluctuations at 2.2 μ , J. Atmos. Terr. Phys. 34:1357.

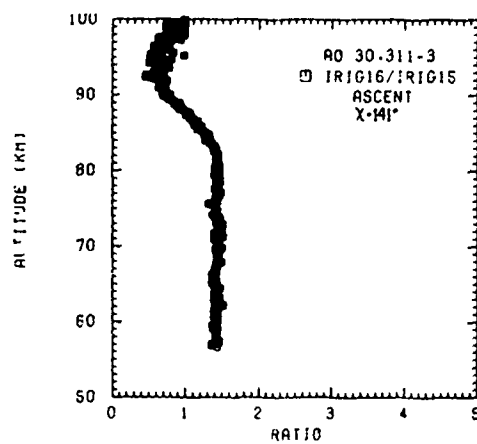
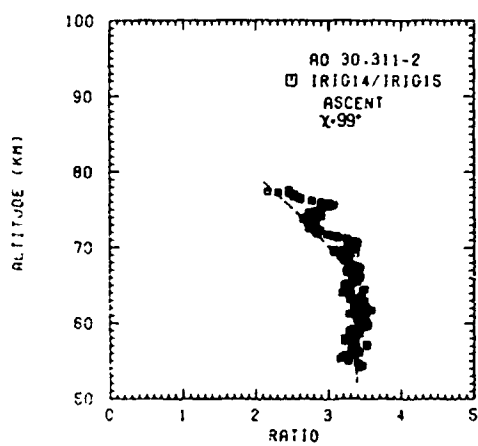
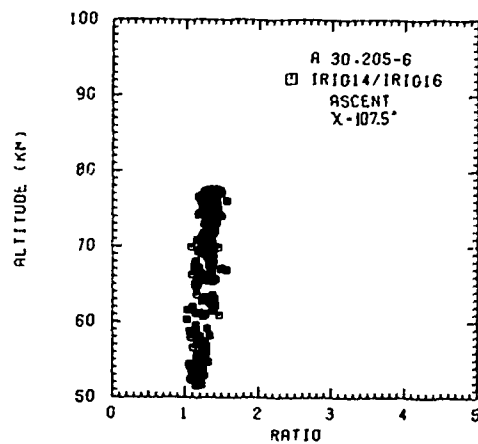
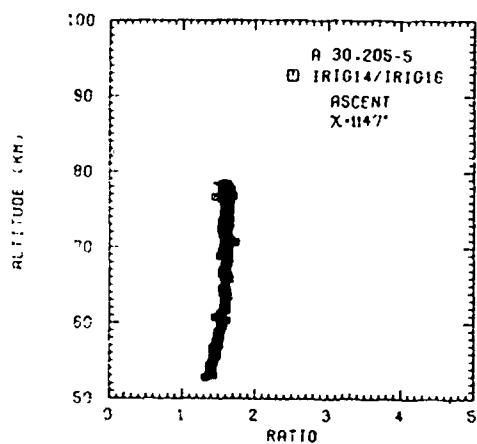


Figure 22. Ratio of Measured Short Wavelength Radiance to Long Wavelength Radiance Versus Altitude for Four Rocket Flights

data shown for rockets A30.205-5 and A30.205-6 (high latitude nighttime flights) are in agreement, showing a slight increase with altitude in the ratio, with values from 1.2 to 1.6. These results do not agree with ratio data reported by Rogers et al¹ for high latitude nighttime measurements where the long wavelength measured intensities were higher than the short wavelength. The discrepancy could be a result of slightly different spectral response characteristics of the Rogers' measurement, even though the reported spectral passbands (1.4 to 1.65 μm and 1.85 to 2.12 μm) seem to be the same as those reported here. The discrepancy is more likely due to the uncertainties in that first measurement, which was really a flight test of the instrument in which lack of time precluded a precise instrument calibration.

The ratio data in Figure 22 for rocket AO30.311-2 (midlatitude twilight flight) show different characteristics than the nighttime data. These data show a higher ratio and considerably more variability. Since the rocket was flown at a time when the earth shadow height was about 60 km ($\chi = 99^\circ$), data above this altitude were probably periodically contaminated by sunlight reflecting into the instrument depending upon the vehicle aspect. This seems to be confirmed by the fact that the short wavelength intensity profile (Figure 20) shows a greater modulation with aspect than the long wavelength profile. In any case, ratio data below 60 km should be unaffected by sunlight. In this altitude region, the ratio is 3.4. If it is now assumed that the minimum ratio values above 60 km are valid, the ratio profile takes on a characteristic of diminishing values with altitude (dashed line in Figure 22) thus implying a markedly different OH production mechanism during twilight than at nighttime.

5.2 Volume Emission Rates

In order to derive volume emission rates from the rocket measured data, it is necessary to correct the measured altitude profiles for aspect (compute zenith profiles) and then differentiate these profiles with respect to altitude, viz.

$$N = -\frac{dR_o}{dh} \quad (6)$$

where

N = volume emission rate (megaphotons/cc-sec)

R_o = zenith radiance (rayleighs)

h = altitude (cm).

This method is applicable only for profiles that traverse the emitting region and for emission regions which are homogeneous, two-dimensionally optically thin, and void of extinction effects such as absorption (van Rhijn regions). The emission criteria can be assumed satisfied for all the hydroxyl data presented, but only rocket AO30. 311-3 provided measurements through the principle hydroxyl emission region. Consequently, only the two emission profiles measured from this rocket were considered for computing volume emission rates.

The first step in the data processing is to derive zenith profiles from the measured data. This requires computation of the instrument viewing angles (α) relative to the local vertical for each measured radiance data point. Unfortunately, the only direct rocket aspect data available is that from the magnetometer and these data alone are not sufficient to derive the aspect angle α . However, the measured radiance data also contains some aspect information. For instance, modulation of the measured radiance data in Figure 21 below the main emission region is indicative of changes in rocket aspect. In fact, the modulation of the radiance data show an in-phase correlation with the magnetometer pitch angle data. If one considers an idealized case where a rocketborne radiometer is flown vertically (with no coning) up to and through a van Rhijn type emission layer, the measured radiance would be a zenith profile. The measured radiance level would be constant up to the bottom of the region and then would diminish as the instrument traversed the layer. Thus, for an actual measurement case where coning and non-vertical trajectory exist and it can be assumed that there are no or at least negligible hydroxyl emissions below some altitude, a measured emission profile that has been properly corrected for aspect (zenith profile) should show a constant radiance level below the layer. A technique based on this idea was devised to correct the measured profiles from rocket AO30. 311-3. In this approach, the magnetometer data were used to compute viewing angles (α) by assuming various headings for the rocket axis of precession. These aspect angles were then used to correct the measured profiles for each heading using the van Rhijn method. The corrected profiles were plotted and compared for the "best fit" to constant radiance below 75 km, and this best fitted profile was then differentiated by a Fourier technique to obtain volume emission rates. The details of this technique follow.

The original measured radiance data files (1660 data points per second) were averaged to obtain one data point every 0.5 km, correlated with altitude and pitch angle. These data are plotted in Figure 23. The pitch angle (P.A.) data were computed using the magnetometer output and Eq. (4) to find angle γ and then pitch angle from

$$P.A. = 180^\circ - \gamma . \quad (7)$$

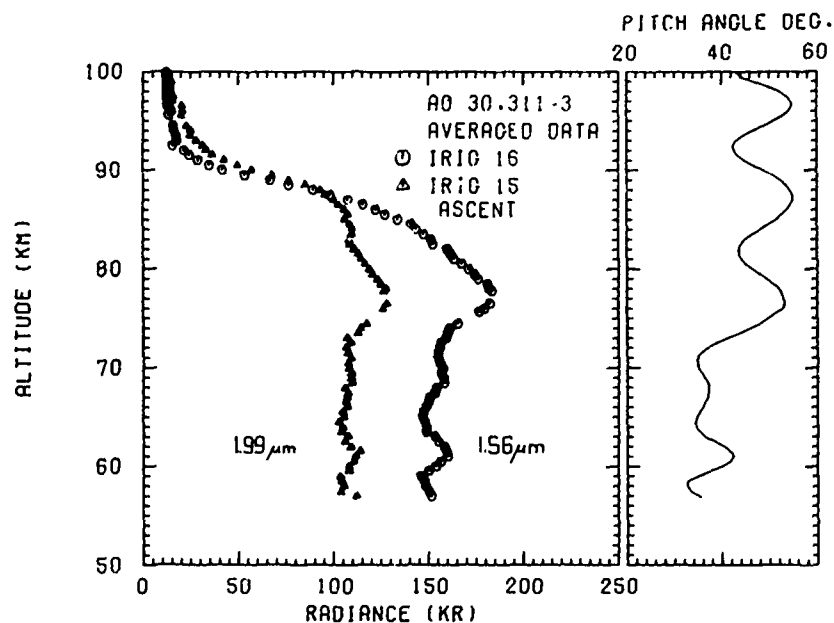


Figure 23. Smooth Radiance Data for the 1.5642- μm and the 1.985- μm Channels Measured on Rocket AO30 311-3. Data not corrected for rocket aspect

The angle (θ_c) between the rocket axis of precession and the earth's magnetic field was determined from the envelope of γ as follows (see Appendix Figure C2):

$$\theta_c = \frac{\gamma_{\max} + \gamma_{\min}}{2} \quad (8)$$

The rocket axis of precession is defined in space by angle θ_c if the heading (Ψ_c) of the axis is known (the position of the earth's magnetic field is assumed to be known). The angle α_c between the local vertical and the axis of precession was computed for several choices of Ψ_c and each data point from (see Appendix C)

$$\alpha_c = \sin^{-1} \left[\frac{lm \pm n \sqrt{m^2 - l^2 + n^2}}{m^2 + n^2} \right] \quad (9)$$

where

$$l = \cos \theta_c$$

$$m = \cos \delta \cos (D - \Psi_c)$$

$$n = \sin \delta$$

$$\Psi_c = \text{heading relative to true north of axis of precession}$$

$$\delta = \text{earth magnetic field dip angle (60}^\circ \text{ for WSMR)}$$

$$D = \text{earth magnetic field declination (+10}^\circ \text{ for WSMR)}.$$

The principal assumption in this calculation is that the heading of the rocket axis of precession does not change during the measurement period from about 53 km to 106 km. Since there is little air drag in this region and no other perturbations such as tip ejections taking place, the assumption is presumed to be valid.

The aspect angle (α) between the local vertical and the rocket axis is derived in detail in Appendix C and is given by

$$\alpha \approx \alpha_c + \theta_c - \gamma. \quad (10)$$

Equation (10) is an approximation based on the assumptions that the radiance data modulation due to coning is in-phase with pitch angle and that the half cone angle (β) is small such that $\cos \beta \approx 1$ and $\sin \beta \approx \beta$. Both of these assumptions were established appropriate for rocket AO30.311-3.

The van Rhijn correction factors (V) were computed from Eq. (11) for each data point and applied to the measured data with Eq. (5) where

$$V_\alpha = \frac{1}{z_2 - z_1} \left[\frac{R_E + z_2}{V_2} - \frac{R_E + z_1}{V_1} \right] \quad (11)$$

where

$$V_1 = \left[1 - \left(\frac{R_E + h}{R_E + z_1} \right)^2 \sin^2 \alpha \right]^{-1/2}$$

$$V_2 = \left[1 - \left(\frac{R_E + h}{R_E + z_2} \right)^2 \sin^2 \alpha \right]^{-1/2}$$

$$V_1 = \text{van Rhijn factor for a thin layer at } z_1$$

$$V_2 = \text{van Rhijn factor for a thin layer at } z_2$$

$$R_E = \text{radius of earth}$$

$$h = \text{height above earth of measurement}$$

z_1 = altitude of lower bound of emitting layer = 76 km

z_2 = altitude of upper bound of emitting layer = 92 km.

In the computation of V_α the rocket altitude (h) replaces the quantity z_1 when $h \geq z_1$, so that $V_1 = \sec \alpha$ whenever the rocket is within the emitting layer. Several zenith profiles were thus computed, one for each assumed heading (Ψ_c). The zenith profile having the best fit to constant radiance below 75 km is shown in Figure 24.

Also shown is aspect angle α .

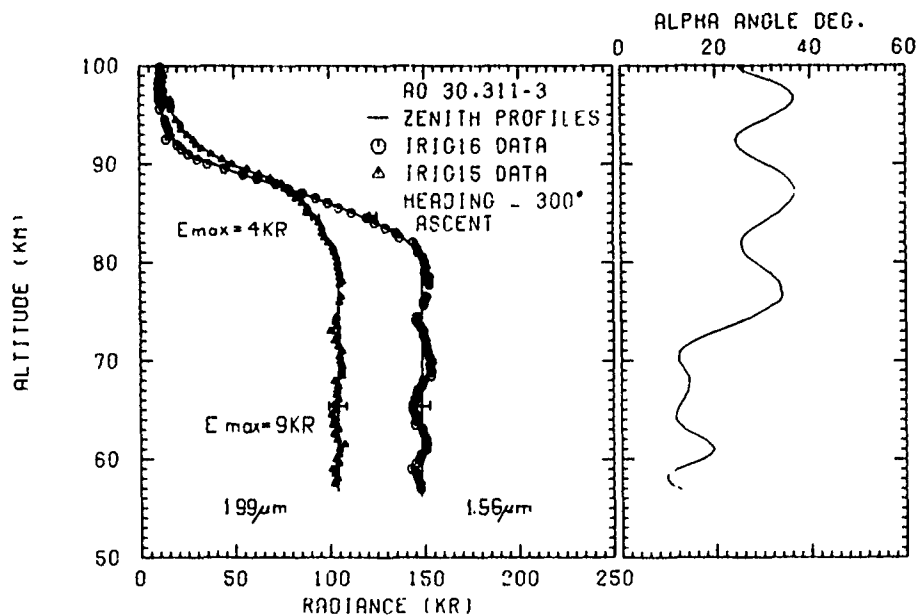


Figure 24. Zenith Altitude Radiance Profiles of the 1.5642- μ m and the 1.985- μ m Channels Computed from Data Measured on Rocket AO30.311-3. Also shown is rocket aspect angle (α) relative to the local vertical

The modulation still present in the zenith profile below the emission layer after the van Rhijn correction (see Figure 24) can be attributed to two assumptions used in deriving Eq. (10). First it is assumed that the half cone angle (β) is constant throughout the flight, and second that the modulation of the uncorrected data is inphase with the pitch angle (P.A.). The error in the aspect angle (α) when Eq. (10) is used, is dependent on the half cone angle (β) and on the difference in heading between the rocket axis (Ψ_c) and the heading of the local earth magnetic field (D). The relationship for the maximum error (e_{\max}) is derived in Appendix C and is given by

$$e_{\max} = \pm \beta \sin \frac{\Omega}{2}$$

where

$$\sin \Omega = \frac{\sin (D - \Psi_c) \cos \delta}{\sin \theta_c}$$

and

- e_{\max} = maximum error in α (degrees)
- β = half cone angle (less than 5° below 76 km and 6° above 76 km)
- Ω = phase angle
- Ψ_c = heading of the axis of precession (300°)
- D = earth magnetic field declination (10° at WSMR)
- δ = earth magnetic dip angle (60° at WSMR)
- θ_c = angle between axis of precession and earth magnetic field.

Below the layer, $\theta_c = 143^\circ$ (see Eq. (8)) so that $e_{\max} = \pm 4.3^\circ$. This means that the angle α used to correct the profile was too large by 4.3° at the minimum radiance values in Figure 24 and too small by 4.3° for the peak radiances shown below 76 km. These corrections were applied to the peak and minimum data points of the radiance modulations in Figure 24. The resulting data points fell within 1 KR of the mean values of 148.4 KR for the $1.56\text{-}\mu\text{m}$ channel and 104.4 KR for the $1.99\text{-}\mu\text{m}$ channel. Consequently, the axis of precession heading of 300° was concluded to be correct. The same technique was applied to the radiance data within the layer where $\theta_c = 131^\circ$ and β was nearly constant at 6° . In this case, $e_{\max} = \pm 3.95^\circ$ and the radiance values corresponding to the peak and minimum pitch angles were similarly corrected. It was found that the actual radiance errors were only of the order of a few kilorayleighs. Thus, it was concluded that the radiance data within the layer were adequately corrected by the initial approximation of α computed from Eq. (10). The final zenith emission profiles were deduced by this analyses and are shown in Figure 24 by the solid lines where the error bar below 76 km is 9 KR, and above 76 km the error bar is about 4 KR.

Computation of volume emission rates by differentiating zenith profile data as defined by Eq. (6) requires sophisticated techniques when digital data are involved. The difficulty arises from the fact that normal random fluctuations between consecutive data points due to telemetry and recorder noise, give rise to large slope changes when simple differentiation is employed. Fitting the data with continuous

functions such as polynomials provide the necessary smoothing of the data points, but this method can overly influence the derivative and thus the volume emission rate computed, depending on the function used. Another technique used by Pearce⁹ and also by Rogers¹ is to smooth the data by Gaussian weights prior to differentiating. This method, though successful, does not take advantage of discriminating against data fluctuations beyond the frequency response of the measuring instrument. The data processing technique selected for results reported here employs derivative digital filtering and Fast Fourier transform to delete data fluctuations outside the instrument frequency response (about 1 Hz) and compute the derivative dR_o/dt . The volume emissions rate (N) was then computed by the chain rule $N = -(dR_o/dt)(dt/dh)$. A complete description of the method is given in Appendix D. In order to provide a large data base for the derivative digital filtering process, the initial data base consisting of 1660 points per second was used. Aspect corrections were applied using the van Rhijn Eqs. (5) and (11), and the viewing angle (α) derived previously.

The volume emission rates were derived in this manner for the two radiometer channels on rocket AO30.311-3 and are shown in Figure 25. The 1.56- μ m emission

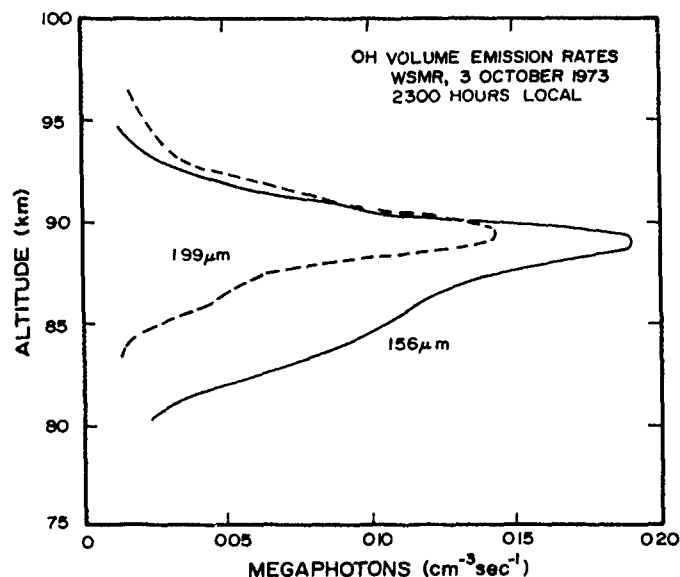


Figure 25. Volume Emission Rates for the 1.5645- μ m and 1.985- μ m Channels Computed From Data Measured on Rocket AO30.311-3

9. Pearce, J.B. (1969) Rocket measurements of nitric oxide between 60 and 95 kilometers, *J. Geophys. Res.* 74:853.

rate shows a peak of 1.9×10^5 photons $\text{cm}^{-3} \text{sec}^{-1}$ at 89 km, while the $1.99\text{-}\mu\text{m}$ emission rate peaks at 1.5×10^5 photons $\text{cm}^{-3} \text{sec}^{-1}$ at 89.5 km. Most of the emission in both wavelength bands come from a narrow layer 8- to 10-km thick, with the largest difference in volume emission rates occurring at and below the altitude of peak emission. In this region, the short wavelength emissions exceed the long wavelength emissions by approximately 6×10^4 photons $\text{cm}^{-3} \text{sec}^{-1}$. Above the peak of the layer, the two emissions are nearly equal.

If the instrument spectral bandpasses were flat and the emissions were constant throughout these spectral regions, the peak volume emission rates (N) per micrometer for each channel would be approximately

$$N(1.56 \mu\text{m}) = 1 \text{ megaphoton cm}^{-3} \text{sec}^{-1} \mu\text{m}^{-1}$$

$$N(1.99 \mu\text{m}) = 0.7 \text{ megaphoton cm}^{-3} \text{sec}^{-1} \mu\text{m}^{-1}.$$

6. CONCLUSIONS

The following conclusions are based solely on the rocketborne radiometer measurements made in the $1.56\text{-}\mu\text{m}$ ($\Delta\lambda = 0.21 \mu\text{m}$) and the $1.99\text{-}\mu\text{m}$ ($\Delta\lambda = 0.20 \mu\text{m}$) infrared bands as described in this report:

- (1) The principal hydroxyl emissions in the bands stated occur in a thin layer 8- to 10-km thick with peak volume emission rates occurring at approximately 89 km.
- (2) There is no conclusive evidence to substantiate any appreciable OH emission layers below 80 km during night conditions in the bands measured.
- (3) The ratio of the nighttime $1.56 \mu\text{m}$ to the $1.99 \mu\text{m}$ overhead radiance is constant at a value of approximately 1.4 up to 80 km regardless of latitude.
- (4) There is some evidence that at twilight the ratio of the $1.56 \mu\text{m}$ to the $1.99 \mu\text{m}$ radiance is larger than 1.4 and diminishes with altitude up to at least 80 km.
- (5) Estimated nighttime peak volume emission rates (N) based on one rocket flight at WSMR are:

$$N(1.56 \mu\text{m}) = 1 \text{ megaphoton cm}^{-3} \text{sec}^{-1} \mu\text{m}^{-1}$$

$$N(1.99 \mu\text{m}) = 0.7 \text{ megaphoton cm}^{-3} \text{sec}^{-1} \mu\text{m}^{-1}.$$

An attempt has been made in this report to document in detail the techniques used in measuring and reducing the rocket radiometer data. On the other hand, little emphasis has been placed on hydroxyl chemistry or comparing the reduced

hydroxyl radiance and volume emission rate data with those reported by other workers in the field. The reasons for this approach were:

(1) Hydroxyl radiometric data reported to date were measured in spectral bandpasses sufficiently different from those reported here such that direct comparison has little meaning.

(2) In much of the radiance data reported in the literature, there is insufficient information on the measuring instrument spectral responses to accurately assess differences in reported results.

(3) A proper analysis of chemical processes was considered beyond the scope of this report, because it involves comparison of the measured data with radiances found by integration of known or modeled spectral OH emissions throughout the spectral bandpasses of the measured data as well as consideration of reaction rates and upper atmospheric composition. The authors feel that sufficient information has been presented in this report to facilitate the accomplishment of the chemistry study mentioned above, but this should be the subject of another report.

References

1. Rogers, J.W., Murphy, R.E., Stair, Jr., A.T., and Ulwick, J.C. (1973) Rocket-borne radiometric measurements of OH in the auroral zone, J. Geophys. Res. 78:7023.
2. Jensen, L.L., Kemp, J.C., and Bell, R.J. (1972) Small Rocket Instrumentation for Measurement of Infrared Emissions, Astrobe D 30.205-3 and Astrobe D 30.205-4, Sci. Rept., No. 3, AFCRL 72-0691, Contract No. F19628-70-C-0302. Utah State University, Logan.
3. Wyatt, C.L., and Kemp, J.C. () Calibration of SWIR Radiometers, Model NR-3B-8, NR-3B-9, NR-3B-10, NR-3B-11, NR-3B-12.
4. Chamberlain, J.W. (1961) Physics of the Aurora and Airglow, Academic Press, New York and London.
5. Huppi, R.J. (1973) Private communication.
6. Baker, D.J. (1974) Rayleigh, the unit of light radiance, Applied Optics 13:2160.
7. Marcou, R.J., and Sullivan, B.J. (1967) Aspects for a Rocket From Magnetometer Data, AFCRL 67-0424, Air Force Cambridge Research Laboratories, Bedford.
8. Peterson, A.W., and Kieffaber, L.M. (1972) Airglow fluctuations at λ 24, J. Atmos. Terr. Phys. 34:1357.
9. Pearce, J.B. (1969) Rocket measurements of nitric oxide between 60 and 95 kilometers, J. Geophys. Res. 74:853.

Appendix A

Selected Rocket Instrument Parameters

1. OH RADIOMETER FIGURES OF MERIT

This appendix includes selected figures of merit describing the OH radiometers (Tables A1 through A4) used on Astrobe D rockets A30.205-5, A30.205-6, AO30.311-1, AO30.311-2, and AO30.311-3 (Figures A1 and A2 for AO30.311-3). The primary reference sources for these data are a series of calibration manuals provided by Wyatt.¹ The data presented applies to all the rocket instruments in general except where noted. For example, the instrument relative spectral response is the same for all rocket instruments, whereas fields-of-view are different for each rocket.

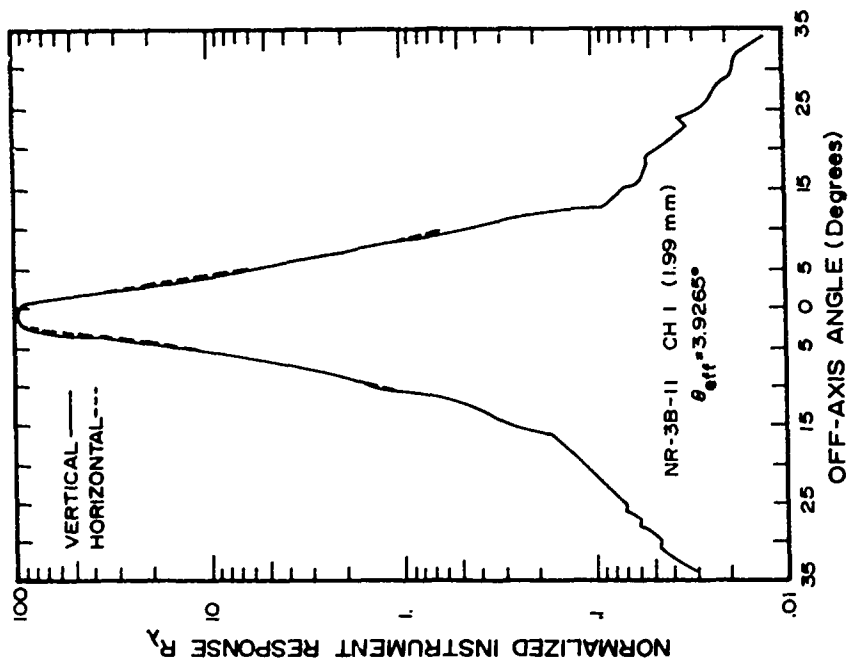


Figure A1. Ortho-Normal Field of View (Rocket AO30.311-3)

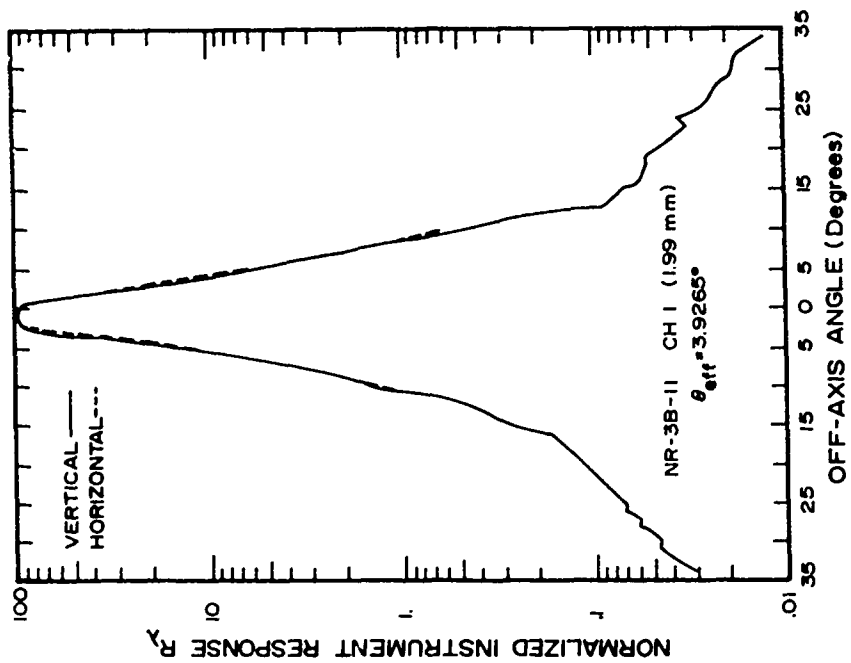


Figure A2. Ortho-Normal Field of View (Rocket AO30.311-3)

Table A1

OH RADIOMETER Channel 2		1.985 MICRONS	
THE INSTRUMENTS RELATIVE SPECTRAL RESPONSE CURVE			
WAVELENGTH (MICRONS)	RELATIVE RESPONSE	WAVELENGTH (MICRONS)	RELATIVE RESPONSE
1.7600	.00	1.7700	.00
1.7800	.01	1.7900	.01
1.8000	.01	1.8100	.04
1.8200	.10	1.8300	.13
1.8400	.19	1.8500	.40
1.8600	.60	1.8700	.46
1.8800	.46	1.8900	.41
1.9000	.71	1.9100	.75
1.9200	.72	1.9300	.75
1.9400	.76	1.9500	.68
1.9600	.53	1.9700	.50
1.9800	.56	1.9900	.77
2.0000	.66	2.0100	1.00
2.0200	.84	2.0300	.72
2.0400	.73	2.0500	.83
2.0600	.83	2.0700	.69
2.0800	.63	2.0900	.70
2.1000	.81	2.1100	.80
2.1200	.58	2.1300	.26
2.1400	.08	2.1500	.02
2.1600	.01	2.1700	.01
2.1800	.01	2.1900	.01
2.2000	.01	2.2100	.01
2.2200	.01	2.2300	.00

Table A2

OH Radiometer Channel 1		1.5642 MICRONS	
THE INSTRUMENTS RELATIVE SPECTRAL RESPONSE CURVE			
WAVELENGTH (MICRONS)	RELATIVE RESPONSE	WAVELENGTH (MICRONS)	RELATIVE RESPONSE
1.3000	.00	1.3100	.00
1.3200	.00	1.3300	.01
1.3400	.01	1.3500	.01
1.3600	.02	1.3700	.02
1.3800	.03	1.3900	.04
1.4000	.06	1.4100	.09
1.4200	.13	1.4300	.20
1.4400	.29	1.4500	.39
1.4600	.47	1.4700	.67
1.4800	.84	1.4900	.90
1.5000	.92	1.5100	.95
1.5200	.96	1.5300	.92
1.5400	.84	1.5500	.84
1.5600	.85	1.5700	.87
1.5800	.91	1.5900	.93
1.6000	.93	1.6100	.95
1.6200	.90	1.6300	.32
1.6400	.84	1.6500	.92
1.6600	1.00	1.6700	.47
1.6800	.11	1.6900	.02
1.7000	.01	1.7100	.01
1.7200	.01	1.7300	.00

Table A3

NR-3B-11	CHANNEL 1	1.985 MICRON	
1.985 MICRON FILTER RESPONSE			
WAVELENGTH (MICRONS)	RELATIVE RESPONSE	WAVELENGTH (MICRONS)	RELATIVE RESPONSE
1.7600	.00	1.7700	.40
1.7800	.50	1.7900	.70
1.8000	1.20	1.8100	4.00
1.8200	9.70	1.8300	12.00
1.8400	17.00	1.8500	37.00
1.8600	54.80	1.8700	41.50
1.8800	41.00	1.8900	36.90
1.9000	63.00	1.9100	67.00
1.9200	63.50	1.9300	66.00
1.9400	66.20	1.9500	58.50
1.9600	45.50	1.9700	42.50
1.9800	47.20	1.9900	61.00
2.0000	80.00	2.0100	83.50
2.0200	70.00	2.0300	59.50
2.0400	60.00	2.0500	68.00
2.0600	67.50	2.0700	56.00
2.0800	51.00	2.0900	56.00
2.1000	64.00	2.1100	62.40
2.1200	45.00	2.1300	20.00
2.1400	6.00	2.1500	1.70
2.1600	1.00	2.1700	.70
2.1800	.70	2.1900	.70
2.2000	.60	2.2100	.60
2.2200	.40	2.2300	.00

Table A4

NR-3B-11		CHANNEL 2	1.5642 MICRON	
1.5624 MICRON FILTER RESPONSE				
WAVELENGTH (MICRONS)	RELATIVE RESPONSE	WAVELENGTH (MICRONS)	RELATIVE RESPONSE	
3.6780	.00	3.6880	.02	
3.6980	.05	3.7080	.08	
3.7180	.10	3.7280	.13	
3.7380	.20	3.7480	.24	
3.7580	.35	3.7680	.43	
3.7780	.60	3.7880	.90	
3.7980	1.30	3.8080	1.96	
3.8180	2.80	3.8280	3.76	
3.8380	4.50	3.8480	6.40	
3.8580	8.00	3.8680	8.62	
3.8780	8.79	3.8880	9.00	
3.8980	9.08	3.9080	8.70	
3.9180	8.00	3.9280	7.87	
3.9380	8.00	3.9480	8.10	
3.9580	8.42	3.9680	8.54	
3.9780	8.47	3.9880	8.60	
3.9980	8.05	4.0080	7.30	
4.0180	7.40	4.0280	8.02	
4.0380	8.65	4.0480	4.00	
4.0580	.90	4.0680	.20	
4.0780	.10	4.0880	.06	
4.0980	.05	4.1080	.00	

Appendix B

Tabulations of Rocket A030.311-3 Data

This appendix contains tabulations of radiance and rocket aspect data as a function of rocket altitude for rocket A030.311-3. The table labeled "Averaged Data" consists of an average of all data points approximately every 0.5 km with spurious data points removed. These data are the input used in computation of the data shown in the table labeled "Zenith Profile." Symbol definitions are as follows:

- ALTITUDE - Rocket altitude (kilometers)
- PITCH - Rocket pitch angle (P. A.) (degrees)
- IRIG 16 - Radiance in the 1.56 μm radiometer channel (kilorayleighs)
- IRIG 15 - Radiance in the 1.99 μm radiometer channel (kilorayleighs)
- RATIO - Ratio of radiance IRIG 16 to IRIG 15
- ALPH - Rocket aspect (viewing angle of radiometer) relative to the local vertical (degrees)

AO 30.311-3 ASCENT
AVERAGED DATA
IRIG 16
IRIG 15

ALTITUDE	PITCH	IRIG16	IRIG15
56.966	35.416	151.503	112.070
57.446	33.501	150.144	103.853
58.020	32.551	148.260	105.497
58.497	32.729	147.535	104.246
58.970	34.772	145.940	103.639
59.534	37.758	150.289	108.497
60.003	40.091	154.112	108.104
60.469	41.702	156.559	110.641
61.024	42.634	160.327	111.641
61.485	41.734	159.494	113.999
61.943	40.697	158.443	109.140
62.490	38.543	155.254	106.068
63.034	36.435	153.224	107.712
63.483	35.474	148.622	104.139
63.931	34.548	148.803	104.854
64.466	34.521	148.187	102.996
64.995	34.875	146.919	105.711
65.523	35.417	147.426	104.997
66.044	36.178	148.948	107.569
66.564	36.567	150.108	106.711
66.999	37.101	150.796	107.247
67.424	37.188	153.261	107.712
67.939	37.346	154.239	106.140
68.447	37.146	158.226	109.784
68.952	36.455	158.044	109.355
69.452	35.907	156.776	109.355
69.950	35.131	157.501	107.925
70.445	34.894	155.970	107.497
70.935	34.762	155.109	109.140
71.502	35.663	155.281	107.783
72.064	37.218	156.124	106.783
72.547	39.040	156.749	109.243
73.023	41.358	159.349	107.283
73.495	43.772	160.182	112.856
73.965	45.793	161.916	114.285
74.431	48.004	165.256	117.295
75.656	51.816	176.780	135.035
75.950	52.916	179.643	126.217
76.484	53.336	182.488	128.199
77.741	52.353	183.412	126.645
78.035	51.918	191.636	127.717
78.469	50.853	188.948	125.802
78.972	49.591	176.946	123.216
79.471	48.885	173.881	120.501
79.964	46.636	170.937	118.768
80.523	45.038	167.750	116.142
81.007	44.112	163.114	113.973
81.485	43.725	161.668	113.142
82.024	43.639	159.902	110.730
82.497	44.055	152.246	108.648

82.962	44.818	151.340	108.319
83.487	46.365	147.236	109.391
84.007	48.193	143.213	109.498
84.519	49.792	140.821	108.640
85.027	51.607	133.891	105.747
85.527	52.620	127.150	107.622
86.122	53.763	122.258	105.640
86.511	54.492	115.408	102.639
86.994	55.032	107.554	100.281
87.470	54.935	98.231	95.458
87.999	54.315	89.044	92.865
88.521	53.484	76.378	84.741
88.977	52.447	66.458	76.382
89.484	50.842	53.123	67.615
89.983	48.843	41.588	56.876
90.474	46.855	34.707	49.696
91.011	44.946	28.944	42.365
91.539	43.368	24.443	36.235
92.006	42.840	21.557	32.870
92.464	42.391	15.246	31.177
92.965	43.057	17.681	28.004
93.505	44.583	17.181	24.796
94.033	46.652	15.898	25.132
94.504	48.868	15.702	22.774
95.550	53.014	13.349	20.277
95.988	54.153	15.025	21.009
96.503	54.793	12.615	20.581
97.003	54.840	12.579	15.758
97.490	53.658	12.252	15.937
98.002	52.111	12.366	14.513
98.498	49.773	12.180	14.365
98.978	46.888	12.180	14.911
99.477	44.047	12.180	13.195
99.857	43.140	12.180	12.400

AO 30.311-3 ASCENT
ZENITH PROFILES
IRIG16
IRIG15
HEADING = 300. DEG.

ALTITUDE	IRIG16	IRIG15	RATIO	ALPHA
56.966	147.934	109.430	1.352	12.461
57.446	147.608	102.099	1.446	10.546
58.020	146.185	104.021	1.405	9.596
58.497	145.394	102.733	1.415	9.774
58.970	142.847	101.443	1.408	11.817
59.534	145.301	104.897	1.385	14.803
60.003	147.271	103.306	1.426	17.136
60.469	148.252	104.771	1.415	18.747
61.024	150.963	105.121	1.436	19.679
61.485	151.004	107.930	1.399	18.779
61.943	150.907	103.950	1.452	17.742
62.490	149.544	102.167	1.464	15.588
63.034	149.004	104.744	1.423	13.480
63.483	145.089	101.663	1.427	12.519
63.931	145.767	102.714	1.419	11.593
64.465	145.178	100.905	1.439	11.565
64.995	143.751	103.432	1.390	11.920
65.523	143.953	102.523	1.404	12.462
66.048	144.999	104.717	1.385	13.223
66.568	145.892	103.714	1.407	13.612
66.999	146.224	103.995	1.406	14.146
67.428	148.556	104.405	1.423	14.233
67.939	149.400	102.809	1.453	14.391
68.447	153.397	106.433	1.441	14.191
68.952	153.677	106.333	1.445	13.500
69.453	152.787	106.573	1.434	12.952
69.950	153.958	105.498	1.459	12.176
70.445	152.369	105.083	1.450	12.166
70.935	151.484	106.590	1.421	12.411
71.504	150.856	104.711	1.441	13.712
72.068	150.344	102.830	1.462	15.639
72.547	149.269	104.075	1.434	17.761
73.023	149.391	100.578	1.485	20.363
73.496	147.397	103.848	1.419	23.047
73.965	145.542	103.302	1.409	25.325
74.431	141.208	103.767	1.409	27.781
75.656	149.602	114.249	1.309	32.193
75.959	149.916	105.331	1.423	33.434
76.484	151.131	106.171	1.423	34.089
77.741	152.705	105.442	1.448	33.635
78.033	151.797	106.736	1.422	33.309
78.469	152.741	105.516	1.448	32.423
78.972	150.342	105.225	1.429	31.351
79.471	150.722	104.451	1.443	29.910
79.964	150.277	104.414	1.439	28.461
80.523	149.034	103.617	1.438	26.855
81.007	146.688	102.517	1.431	25.937
81.485	145.858	102.077	1.429	25.550
82.028	144.368	99.973	1.444	25.464
82.497	136.978	97.745	1.401	25.880
82.962	135.270	96.817	1.397	26.643

83.487	129.772	96.416	1.346	28.190
84.007	124.003	94.810	1.398	30.018
84.519	119.919	92.515	1.296	31.617
85.027	111.737	88.750	1.266	33.432
85.527	104.857	88.753	1.181	34.445
86.027	99.423	85.909	1.157	35.588
86.511	92.991	82.701	1.124	36.317
86.994	86.057	80.238	1.073	36.857
87.477	78.698	76.476	1.029	36.760
87.999	71.910	74.996	.959	36.140
88.521	62.329	69.153	.901	35.309
88.977	54.919	63.120	.870	34.272
89.484	44.720	56.919	.786	32.667
89.983	35.772	48.921	.731	30.668
90.474	30.449	43.599	.698	28.680
91.011	25.842	37.824	.683	26.771
91.539	22.118	32.788	.675	25.193
92.006	19.621	29.919	.656	24.465
92.464	13.904	28.433	.489	24.216
92.965	16.040	25.405	.631	24.882
93.505	15.388	22.209	.693	26.408
94.033	13.975	22.091	.633	28.477
94.504	13.503	19.584	.689	30.693
95.550	10.956	16.643	.658	34.839
95.988	12.159	17.002	.715	35.978
96.503	10.125	16.519	.613	36.618
97.003	10.116	12.673	.798	36.465
97.490	9.977	12.977	.769	35.483
98.002	10.260	12.041	.852	33.936
98.498	10.374	12.235	.848	31.598
98.978	10.682	13.077	.817	28.713
99.477	10.959	11.873	.923	25.872
99.857	11.042	11.241	.982	24.965

Appendix C

Rocket Aspect From Magnetometer Data

A magnetometer responds to the effective magnetic field component parallel to its sensing axis as follows:

$$v = V_b + \frac{B}{k} \quad (C1)$$

where

v = voltage output from magnetometer due to field B

B = instantaneous effective magnetic field intensity component aligned with the magnetometer axis (milligauss)

V_b = bias voltage (volts) (voltage output from magnetometer when $B = 0$)

k = calibration factor (milligauss/volt).

Magnetometers are calibrated by applying known fields to the instruments in a controlled field environment and measuring the output voltage. The bias voltage V_b and calibration factor k are determined from these data (see Figure C1). Equation (C1) is valid only in the linear portion of the calibration curve shown in Figure C1.

In rocket research, magnetometers are used in the payloads to determine rocket spin and precession (coning) relative to the earth's magnetic field. In this application, the contribution to the effective magnetic field acting on the magnetometer from the earth's magnetic field is

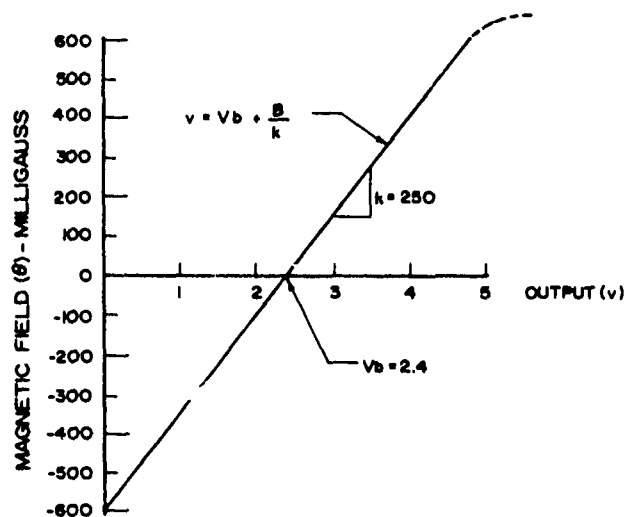


Figure C1. Typical Magnetometer Calibration Data
(Schonstedt Instrument Company)

$$B_1 = B_0 \cos \phi \quad (C2)$$

where

B_1 = component of earth's field aligned with the magnetometer axis

B_0 = total field intensity of earth's magnetic field

ϕ = instantaneous angle between earth's total field and magnetometer axis

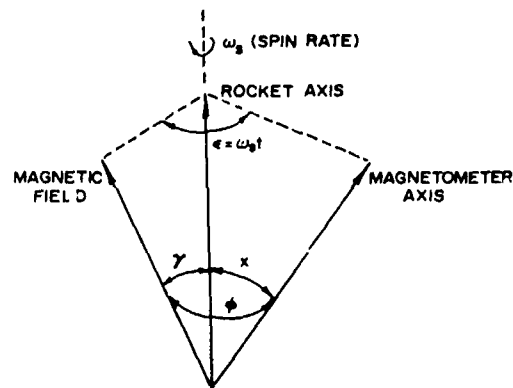
Let ΔB be the field intensity aligned with the magnetometer axis arising from currents in the payload so that the net effective field B acting on the magnetometer is

$$B = B_1 + \Delta B = B_0 \cos \phi + \Delta B \quad (C3)$$

Combining Eq. (C3) and C1) yields the instantaneous voltage output from the magnetometer due to all fields

$$v = V_b + \frac{\Delta B}{k} + \frac{B_0}{k} \cos \phi \quad (C4)$$

For a 90° magnetometer (magnetometer axis perpendicular to rocket axis), the $\cos \phi$ is related to spin and coning of the rocket as follows (see Figure C2)



$$\cos \phi = \cos \alpha \cos X + \sin \alpha \sin X \cos \omega_s t$$

FOR 90° MAGNETOMETER $X = 90^\circ$
AND $\cos \phi = \sin \gamma \cos \omega_s t$

Figure C2. Magnetometer Geometry for Spinning Rocket in a Magnetic Field

$$\cos \phi = \sin \gamma \cos \omega_s t \quad (C5)$$

where

γ = instantaneous angle between the rocket axis and the earth's magnetic field

ω_s = spin radian frequency.

Combining Eq. (C5) and (C4) yields the instantaneously voltage output of the magnetometer in terms of spin and coning

$$v = V_b + \frac{\Delta B}{k} + \frac{B_o}{k} \sin \gamma \cos \omega_s t \quad (C6)$$

Since $\sin \gamma$ (representative of coning) is a slowly varying function in time compared to $\cos \omega_s t$ (the spin function), Eq. (C6) is an amplitude modulated waveform (see Figure C3). The envelope of the carrier is defined by two equations derived from Eq. (C6) when $\cos \omega_s t = +1$ and -1 respectively

$$v_u = V_b + \frac{\Delta B}{k} + \frac{B_o}{k} \sin \gamma \quad (C7)$$

$$v_l = V_b + \frac{\Delta B}{k} - \frac{B_o}{k} \sin \gamma \quad (C8)$$

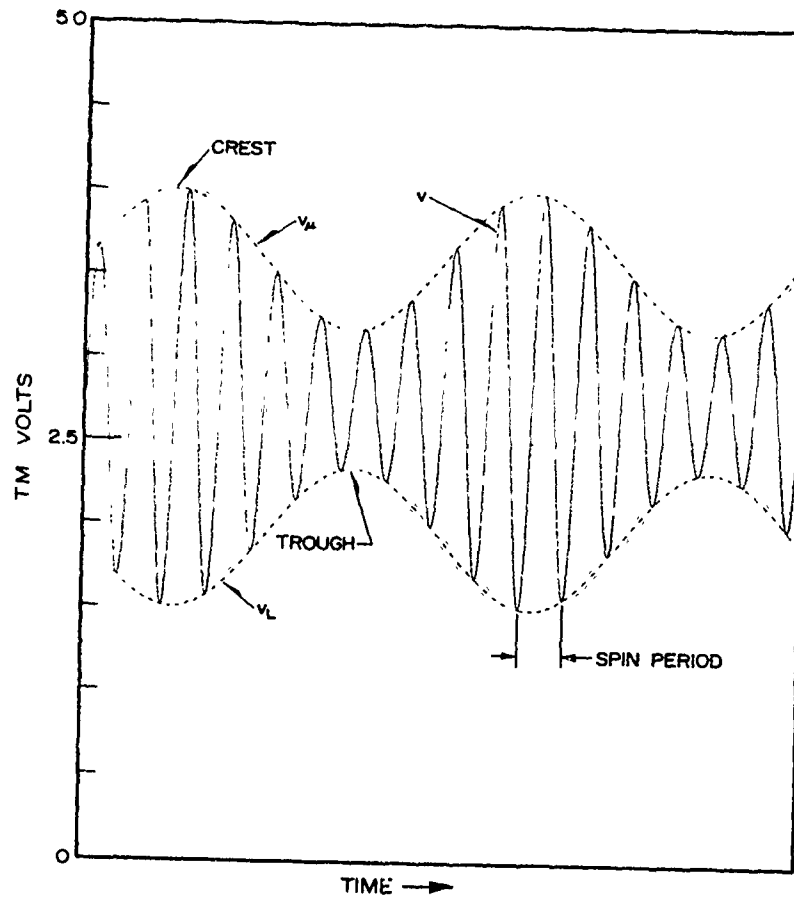


Figure C3. Schematic Showing Typical Magnetometer TM Volts Versus Flight Time. v_u = upper voltage envelope, v_l = lower voltage envelope, v = instantaneous magnetometer output

where

v_u = upper envelope voltage

v_l = lower envelope voltage.

The average value of the envelope voltage at any instant of time is

$$v_{ave} = \frac{v_u + v_l}{2} = V_b + \frac{\Delta B}{k} \quad (C9)$$

Using Eq. (C9) in Eq. (C6) yields

$$v = v_{ave} + \frac{B_0}{k} \sin \gamma \cos \omega_s t \quad (C10)$$

Likewise, the envelope Eq. (C7) and (C8) become

$$\begin{aligned} v_u &= v_{ave} + \frac{B_o}{k} \sin \gamma \\ v_l &= v_{ave} - \frac{B_o}{k} \sin \gamma \end{aligned} \quad (C11)$$

Notice that v_u approaches v_l only when γ approaches 0 or 180° . This condition occurs only when the rocket axis is aligned with the magnetic field. Using Eq. (C11) and the rocket magnetometer output voltage data (v_u and v_l), the rocket aspect angle (γ) relative to the earth's magnetic field can be found from

$$\gamma = \sin^{-1} \left[\frac{k}{2B} (v_u - v_l) \right] \quad (C12)$$

In the northern hemisphere, the angle γ is usually greater than 90° and it is common practice to describe rocket motion in terms of pitch angle. Pitch angle (P.A.) is defined as follows:

$$P.A. = 180 - \gamma \quad (C13)$$

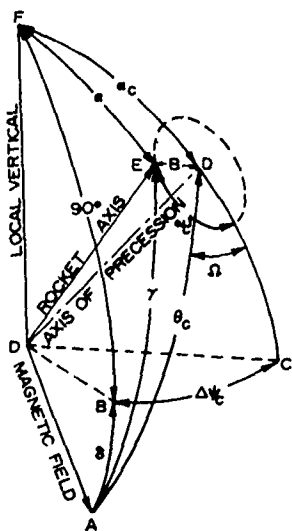


Figure C4. Spherical Geometry of Coning Rocket

For optical/infrared rocket measurements, it is important to know the rocket aspect with respect to the local vertical so that the instrument viewing angle relative to the vertical can be determined. From the geometry shown in Figure C4 (spherical triangle AEFA), it can be seen that

$$\cos \gamma = \cos \delta \sin \alpha \cos (D - \psi) - \sin \delta \cos \alpha \quad (C14)$$

where

γ = angle between rocket axis and earth's magnetic field

α = angle between rocket axis and the local verticle

δ = local earth's magnetic field dip angle (inclination)

D = local earth's magnetic field declination angle

ψ = azimuth of rocket axis relative to true north.

Equation (C12) can be solved for $\sin \alpha$ as follows:

$$\sin \alpha = \frac{ab \pm c \sqrt{b^2 - a^2 + c^2}}{b^2 + c^2} \quad (C15)$$

where

$$a = \cos \gamma$$

$$b = \cos \delta \cos (D - \psi)$$

$$c = \sin \delta$$

Since the earth's magnetic field parameters δ and D are usually known, Eq. (C15) can be solved for the desired rocket aspect angle (α) provided the rocket heading (ψ) is known. In most actual cases, the rocket heading (ψ) is continually changing with time as the rocket precesses (cones) so unless other data (such as gyro data) are available, it is difficult to prescribe the variations in rocket heading. A more practical expression for α can be derived in terms of the terms of the rocket axis of precession since the heading of this axis is not as susceptible to change.

To derive this relationship, the angle α is defined in terms of the angle (θ_c) between the magnetic field and the rocket axis of precession and the coning half angle (β). If it is assumed that the rocket coning is sinusoidal, then from the geometry of Figure C4 (spherical triangle AEDA)

$$\cos \gamma = \cos \theta_c \cos \beta + \sin \theta_c \sin \beta \cos (\omega_c t - \Omega) \quad (C16)$$

where

γ = angle between rocket axis and earth's magnetic field

θ_c = axis of precession (coning) relative to the earth's magnetic field

β = half cone angle

ω_c = coning radian frequency

t = time

Ω = phase angle.

The maximum and minimum values of γ can be found from Eq. (C16) when $\cos (\omega_c t - \Omega) = -1$ and $+1$ respectively, thus

$$\gamma_{\max} = \theta_c + \beta$$

$$\gamma_{\min} = \theta_c - \beta \quad (C17)$$

Both β and θ_c can be found from knowledge of γ and Eq. (C17) as follows:

$$\beta = \frac{\gamma_{\max} - \gamma_{\min}}{2}$$

$$\theta_c = \frac{\gamma_{\max} + \gamma_{\min}}{2} \quad (C18)$$

From geometry in Figure C4 (see spherical triangle ADFA),

$$\cos \theta_c = \cos \delta \sin \alpha_c \cos (D - \psi_c) - \sin \delta \cos \alpha_c \quad (C19)$$

which can be solved for $\sin \alpha_c$

$$\sin \alpha_c = \frac{l \pm m \pm n \sqrt{m^2 - l^2 + n^2}}{m^2 + n^2} \quad (C20)$$

where

$$l = \cos \theta_c$$

$$m = \cos \delta \cos (D - \psi_c)$$

$$n = \sin \delta$$

$$\psi_c = \text{azimuth of axis of precessions relative to true north.}$$

$$\alpha_c = \text{angle of axis of precession relative to local vertical.}$$

All other symbols have been defined previously.

The phase angle (Ω) in Eq. (C16) and shown in Figure C4 can be described in terms of the heading (ψ_c) of the precession axis as follows. Referring to Figure C4, the spherical right triangle ADFA yields

$$\frac{\sin (90 + \delta)}{\sin (180 - \Omega)} = \frac{\sin \theta_c}{\sin \Delta \psi_c}$$

which reduces to

$$\sin \Omega = \frac{\sin \Delta\psi_c \cos \delta}{\sin \theta_c} \quad (C22)$$

where

$$\Delta\psi_c = D - \psi_c$$

All other symbols have been defined previously. The phase angle can also be derived in terms of α_c , θ_c and $\Delta\psi_c$ where

$$\cos \Omega = \frac{\cos \delta \cos \Delta\psi_c - \cos \theta_c \sin \alpha_c}{\sin \theta_c \cos \alpha_c} \quad (C23)$$

The aspect angle (α) of the rocket axis relative to the local vertical is (see Figure C4) spherical triangle EDFE where

$$\cos \alpha = \cos \alpha_c \cos \beta - \sin \alpha_c \sin \beta \cos \omega_c t \quad (C24)$$

In many actual cases, the half cone angle (β) is small such that the following approximations are possible:

$$\cos \beta \approx 1$$

$$\sin \beta \approx \beta \quad (C25)$$

For this case, Eq. (C24) and (C16) become

$$\cos \alpha \approx \cos \alpha_c - \beta \sin \alpha_c \cos \omega_c t \quad (C26)$$

or

$$\alpha \approx \alpha_c + \beta \cos \omega_c t \quad (C27)$$

$$\cos \gamma \approx \cos \theta_c + \beta \sin \theta_c \cos (\omega_c t - \Omega) \quad (C28)$$

or

$$\gamma \approx \theta_c - \beta \cos (\omega_c t - \Omega) \quad (C29)$$

If the additional approximation can be made that the phase angle (Ω) is small and can be neglected (see Eq. C23), then $\beta \cos \omega_c t$ can be eliminated from Eq. (C27) and (C29) to yield

$$\alpha \approx \alpha_c + \theta_c - \gamma \quad . \quad (C30)$$

The error (ϵ) encountered by using the approximation (Eq. (C30)) can be derived by adding Eq. (C27) and (C29) and making use of the identity

$$\cos \omega_c t - \cos (\omega_c t - \Omega) = -2 \sin (\Omega/2) \sin (\omega_c t - \Omega/2) \quad .$$

The instantaneous error (ϵ) is

$$\epsilon = -2\beta \sin (\Omega/2) \sin (\omega_c t - \Omega/2) \quad (C31)$$

and thus the maximum error (ϵ_{\max}) is

$$\epsilon_{\max} = \pm 2\beta \sin \frac{\Omega}{2} \quad . \quad (C32)$$

For many cases of well behaved free ballistic rocket flight, the angles defining the rocket axis of precession, α_c and θ_c , are constant for at least some portions of flight. For these cases, a convenient expression can be found for rocket aspect α using Eq. (C30) and (C13):

$$\alpha \approx \text{P.A.} + \text{Constant} \quad (C33)$$

where

$$\text{Constant} = \alpha_c + \theta_c - 180^\circ \quad .$$

Equation (C32) is particularly useful since the maximum angular error can be estimated by Eq. (C32). The procedure for evaluating Eq. (C33) follows:

- (1) Compute the angle γ and P.A. using the magnetometer data and Eqs. (C12) and (C13).
- (2) Compute θ_c and β from the time history of γ found in step (1) using Eq. (C18).
- (3) Compute α_c from θ_c and a known or estimated value of ψ_c (heading of the axis of precession using Eq. (C20)).
- (4) Compute the estimated aspect angle α from α_c and θ_c and the P.A. data found in (1) above using the approximation Eq. (C33). The maximum angular error in α can be found by evaluating Eq. (C22) and (C32).

It must be pointed out that there is an additional error in aspect angle α not accounted for by Eq. (C31) and this arises from the assumption that the cone angle β is small. This can be illustrated by an example where the heading of the rocket axis of precession coincides the heading of earth magnetic field, that is $\psi_c = D$. For this case

$$\alpha_c + \theta_c = 90^\circ + \delta$$

and Eq. (C33) reduces to

$$\alpha = P.A. + \delta - 90^\circ,$$

where δ is the magnetic field dip angle. Also, for this case Eq. (C22) indicates that $\Omega = 0$ and thus Eq. (C32) would yield a maximum error of 0° . This result is obviously incorrect but for cases where β is small ($\leq 6^\circ$), the discrepancy can be shown to be negligible for most applications. For instance, assume a measured P.A. to be 50° at WSMR ($\delta = 60$, $D = 10$) and $\beta = 6^\circ$. The approximation for α yields $\alpha = 20^\circ$. On the other hand, Eq. (C15) can be solved for α without approximation. For the worst case the instantaneous rocket axis heading (ψ), as distinguished from the axis of precession heading (ψ_c), differs from the magnetic field heading (D) by the half cone angle (β); that is

$$D \pm \beta = \psi.$$

When Eq. (C15) is evaluated under these conditions, the value of α is 20.07° - a discrepancy of only 0.07° .

Appendix D

Derivative Using Numerical Filtering*

A numerical filter generally consists of a set of weights $w(n)$ applied to a set of input data (see I below) points $X(t)$ to form a "filtered" set of data $Y(t)$.

For this problem, an imperical number N was set and a low pass-derivative filter was calculated and applied to the data as follows:

$$Y(t) = \sum_{n=N}^N w(n) X(n + t) \quad . \quad I$$

The values of $w(n)$ were calculated as follows: An array of 8192 values of frequency response versus frequency $W(f)$ was set up on the computer. The array consisted of 8192 complex values at equally spaced data values from $-4095 \Delta f$ to $4096 \Delta f$ where

$$f = \frac{1}{8192 \Delta t}$$

and Δt is the time spacing of the input data. The value at each frequency (f) was $-(2\pi f)i C(f)$, where $-(2\pi f)i$ represents the time (t) derivative of $e^{-(2\pi f)i t}$ divided by $e^{-(2\pi f)i t}$ and $C(f)$ is the response curve used. For this procedure:

* This analysis has been accomolished by Niel Grossbard of Boston College for AFCRL Data Computer Center.

$$\begin{aligned}
C(f) &= 1 && \text{for } |f| \leq f_{\min} \\
&= 1/2 \cos \frac{2\pi(|f| - f_{\min})}{(f_{\max} - f_{\min})} + 1 && \text{for } f_{\min} < |f| < f_{\max} \\
&= 1 && \text{for } |f| \geq f_{\max}
\end{aligned}$$

where f_{\min} and f_{\max} are imperical input frequencies.

The time series representation of $W(f)$, $(U(t))$ was then derived using a numerical Fast Fourier Transform. The results for $U(-N \Delta t)$ to $U(+N \Delta t)$ formed the $w(n)$ between $-N$ and $+N$ used in the computer program to calculate dl_0/dt .

The resultant filtering only approximates the frequency response function $C(f)$ for two reasons. The first reason is the truncation of $U(t)$ such that $W(n) = 0$ for $|n| > N$. This "error" minimized by increasing N until the final results of the program did not change by 1 percent with increasing N . The second reason is that the function is only set at the values $n \Delta f$ for $n = -4095$ to 4096 and not at frequency values falling between these points. This problem was minimized by using many values (8192) in $W(f)$ and by using a "smooth" $C(f)$. In particular, the behavior of $C(f)$ between f_{\min} and f_{\max} was set up to form a "smooth" change from a derivative response to a zero response. This error was not checked but experience indicates that this error should be less than 3 percent for the parameters used. In any case, the errors due to the inaccuracy in fitting $C(f)$ are probably less than the error in assuming $C(f)$ specifies the necessary frequency response curve for reducing $X(t)$.

Using this analysis, we find dR_0/dt . These results were transformed to dR_0/dh as follows:

Let $Z(t)$ be the series of values of dR_0/dt with corresponding time array $tt(n)$ and height array $h(t)$ and V_{eff} array. $V_{\text{eff}}(t)$.

$$N_z(h(t)) = - \frac{1}{V_{\text{eff}}(t)} \quad Z(t) = \frac{tt(t+1) - tt(t-1)}{h(t+1) - h(t-1)}$$

where

$$\frac{tt(t+1) - tt(t-1)}{h(t+1) - h(t-1)}$$

is used to approximate $\frac{dt}{dh}$ and the chain rule

$$\frac{dR}{dh} = \frac{dR}{dt} \frac{dt}{dh}$$

has been used. This approximation for dt/dh is another small source of error in the values of $N_z(h(t))$. This error should be minimized by the slow change of $h(t)$ and $tt(t)$ in the input data.

In order to make an estimation of the error in $N_z(h(t))$, the following procedure was used:

To find the error for $N_z(h(t))$ consider

$$\frac{N_z(h(t-1)) + N_z(h(t)) + N_z(h(t+1))}{3} = N_{zM}(h(t))$$

$$\sigma_{N_{zM}}(h(t)) = \sqrt{\frac{\sum_{j=t-1}^{t+1} (N_z(h(j)) - N_{zM}(h(t)))^2}{2}}$$

Then it is assumed the correct answer for $N_{zc}(h(t))$ ($N_{zM}(h(t))$) lies in the region

$$N_{zM}(h(t)) - \sigma_{N_{zM}}(h(t)) \leq N_{zc}(h(t)) \leq N_{zM}(h(t)) + \sigma_{N_{zM}}(h(t))$$

with a probability ~ 0.68 .

This procedure should give an overestimate of the error if the results of $N_z(h(t))$ are unbiased since any change between $N_{zc}(h(t-1))$, $N_{zc}(h(t))$ and $N_{zc}(h(t+1))$ tends to increase calculated value of $\sigma_{N_{zM}}(h(t))$. At the turning points of the $N_{zc}(h(t))$, however, this method tends to underestimate the strength of the peak.